Capacitive Position-Sensing and Electronics

for a Linear Electrostatic Micromotor

by

Lily Y. Kim

S.B. Massachusetts Institute of Technology (June 1997)

Submitted to the Department of Electrical Engineering and Computer Science
in Partial Fulfillment of the Requirements for the Degree of

Master of Engineering in Electrical Engineering and Computer Science

at the

Massachusetts Institute of Technology

May 20, 1998

Author_____
Department of Electrical Engineering and Computer Science
May 20, 1998

Certified by___
Jeffrey H. Lang
Thesis Supervisor

Accepted by_____
Arthur C. Smith
Chairman, Department Committee on Graduate Theses

Capacitive Position-Sensing System and Electronics
for a Linear Electrostatic Micromotor
by
Lily Y. Kim

Submitted to the
Department of Electrical Engineering and Computer Science

May 20, 1998

In Partial Fulfillment of the Requirements for the Degree of
Master of Engineering in Electrical Engineering and Computer Science

ABSTRACT

Over the past ten years, many designs for electrostatic micromotors have emerged. Recently, a new linear electrostatic micromotor has been designed which, unlike most micromotors, is purposefully actuated by both in-plane and out-of-plane forces. However, using repulsive out-of-plane forces introduces an instability into the motor. This instability must be corrected using closed-loop control, which becomes an essential part of the design. In this thesis, a milli-scale model of the new micromotor is built to test the design in a low-cost manner. All electronics for the model are also designed and built, including high-voltage drive circuitry, position-sensing circuitry, and an RC network to interface the electronics to the motor itself. Using the position-sensing circuitry and the milli-scale motor, a capacitive position-sensing scheme is experimentally demonstrated for detecting the motor position in two directions: in-plane and out-of-plane. The in-plane position measurement accuracy is roughly 0.06 mm.

Thesis Supervisors: Carl Taussig, Hewlett-Packard Research Laboratories
Jeff Lang, Associate Director of MIT LEES

Acknowledgments

Working on this thesis was an educational and rewarding experience because of the many people who helped me along the way.

First, I would like to thank Carl Taussig, my mentor and supervisor at Hewlett-Packard Research Labs. Daily, he took the time to discuss problems and to give thoughtful advice. I especially appreciate all the interesting and fun discussions we had, which extended beyond technical matters. I would also like to thank other people at Hewlett-Packard, especially C.C. Yang, Graeme Burward-Hoy, Lennie Kiyama, and Sui-hing Leung for their advice and encouragement.

I also want to thank Professor Jeffrey Lang, my thesis supervisor at MIT. He provided a fresh viewpoint on the project and helped me to look at things from new angles. I also thank Professor Stephen Senturia for introducing me to the MEMS area during my undergraduate years, and guiding and supporting me during my graduate year.

This project was performed at and sponsored by Hewlett-Packard Research Labs as part of the VI-A program. I would like to thank Professor Markus Zahn and Lydia Wereminski at MIT, Rick Baer at Hewlett-Packard, and the rest of the VI-A program for giving me the opportunity to learn about the world of engineering in industry.

Finally, I express my gratitude to my mother, father, and sister, Connie, who have always been there for me.

Table of contents

1.0 Introduction

The idea of making micron-scale electrostatic motors using integrated circuit fabrication technology has existed for over a decade. In that time, many different micromotor designs have emerged. [1-2] This thesis explores a new linear electrostatic micromotor purposefully actuated by both in-plane and out-of-plane forces. Two main parts, a movable rotor and a fixed stator, constitute the motor. The rotor and stator are parallel, insulating plates on which metal electrodes have been printed. When these electrodes are set at certain voltages, electrostatic forces are created in two orthogonal directions, moving the rotor. Although this motor design incorporates concepts from past designs, it is unique because it combines electrostatic repulsion, closed-loop control, and position-sensing in a new way.

One advantage of this design is that it uses repulsive out-of-plane forces to help prevent the rotor from crashing into the stator. However, when the repulsive forces are used, an instability in the rotor's in-plane equilibrium is created. To counteract this instability, an active control system must be implemented. In its final incarnation, the motor is meant to be fabricated on micron scale. However, to test the design at low cost, large-scale prototypes. All experiments in this thesis deal with one of these millimeter scale models.

Prior to this thesis, the motor was designed by Carl Taussig of Hewlett-Packard Research Labs, who also performed preliminary force and position-sensing measurements on a first-generation milli-scale motor prototype. Taussig also designed the motor prototype and mechanical setup used during this thesis project. The motor prototype is shown at the far right in Figure 1.1, which depicts a block diagram of the motor and its control system .
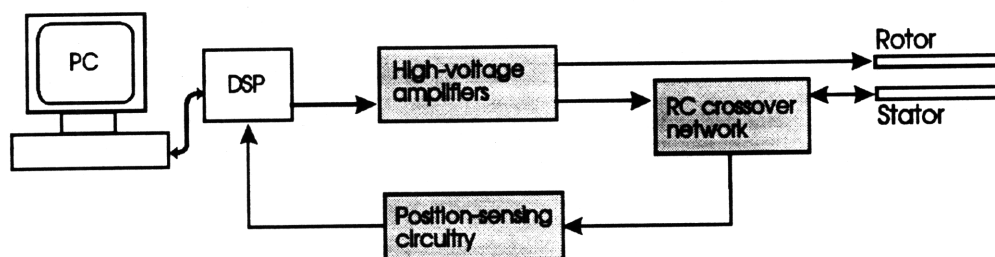
Figure 1.1: Block diagram of control system; thesis work in gray

The gray blocks of Figure 1.1 represent hardware that was designed and built during this thesis.

They show the electronics that were designed for the motor: 1) position-sensing circuitry to condition the feedback signal, 2) high-voltage amplifiers to drive the motor, and 3) an RC crossover network to connect the position-sensing circuitry and the high-voltage amplifiers to the motor itself. In addition, a DSP (digital signal processor) would be needed to perform the actual control algorithm to determine the stator voltages. Using the position-sensing circuitry and the mini-scale motor, a capacitive position-sensing scheme was experimentally demonstrated for detecting the motor position in two directions: in-plane and out-of-plane.

This thesis is organized as follows. Chapter 2 describes the general motor design, principles of operation, and related research. Chapter 3 describes the specific motor implementation (milli-scale model) that was used during this project. The position-sensing circuitry, high-voltage circuitry, and RC network are discussed in Chapters 4, 5, and 6, respectively. Finally, Chapter 7 concludes with a summary and suggestions for future work.

2.0 Background

2.1 Previous work on this design

The micromotor design explored in this thesis was created by Carl Taussig of Hewlett-Packard Research Laboratories [3] and is described below. To test the motor's principles of operation, Taussig also performed several experiments, described in Section 2.1.3. This thesis differs from those experiments because it is a step toward a complete, integrated prototype, going beyond testing isolated concepts.

2.1.1 Motor's physical description

The motor is composed of two main pieces, a rotor and stator, shown below in Figure 2.1.
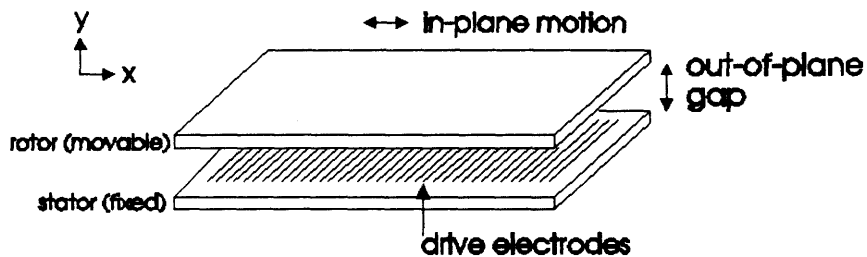
Figure 2.1: Basic motor

Physically, both pieces are similar, however they differ in function. Each piece is a flat insulating plate with parallel conducting strips (drive electrodes) on one face and a ground plane on the opposite face. The rotor and stator are placed so their planes are parallel and their electrodes are facing each other (thus, the rotor electrodes cannot be seen in the figure). During operation, the stator remains fixed in place, while the rotor moves in a straight line, as shown in Figure 2.1. The out-of-plane distance between the rotor and stator is called the rotor-stator gap.

Because Figure 2.1 is merely a sketch, it leaves out some details. First, the rotor does not levitate in mid-air, as shown in the figure. The rotor must be suspended by supports which are very flexible in the in-plane direction. The characteristics of these supports are important for determining how gravity affects the rotor. Second, although Figure 2.1 shows the rotor and stator as being the same size, the stator is actually larger and has a greater area covered by electrodes. This allows all of the rotor electrodes to be useful throughout a range of in-plane motion.

The drive electrodes are each assigned to a group in a periodic fashion, shown in Figure 2.2. In this thesis, the electrodes have been divided into groups of four. All electrodes of the same group are electrically connected. These groups are called the phases of the motor. The electrode width and spacing are the same for both rotor and stator. The motor's phases are depicted in Figure 2.2, which shows an 8-electrode-wide piece of the motor's cross-section.
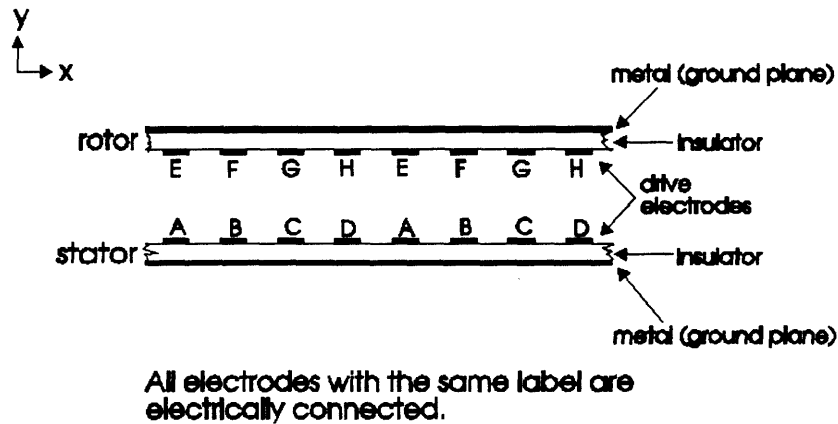
Figure 2.2: Motor phases: electrode grouping

2.1.2 Motor function

There are a few aspects of the motor's functioning which, when combined, make it a unique design. First, the motor can generate both in-plane and out-of-plane forces. Second, the motor uses closed-loop control to take advantage of the repulsive out-of-plane forces. Third, the motor uses a position-sensing scheme in which the drive-electrodes are used as position-dependent capacitors. The rotor's position can be measured by sensing changes in capacitance.

Electrostatic forces

To actuate the motor, certain patterns of voltage must be applied to the rotor and stator phases. These voltage patterns cause electric fields to take a certain shape, in turn causing forces on the rotor in the x (in-plane) and y (out-of-plane) directions. For example, if voltages are applied to the rotor and stator as shown in Figure 2.3a, the forces in the x and y directions which

result are those shown as a function of rotor displacement in Figure 2.3b.
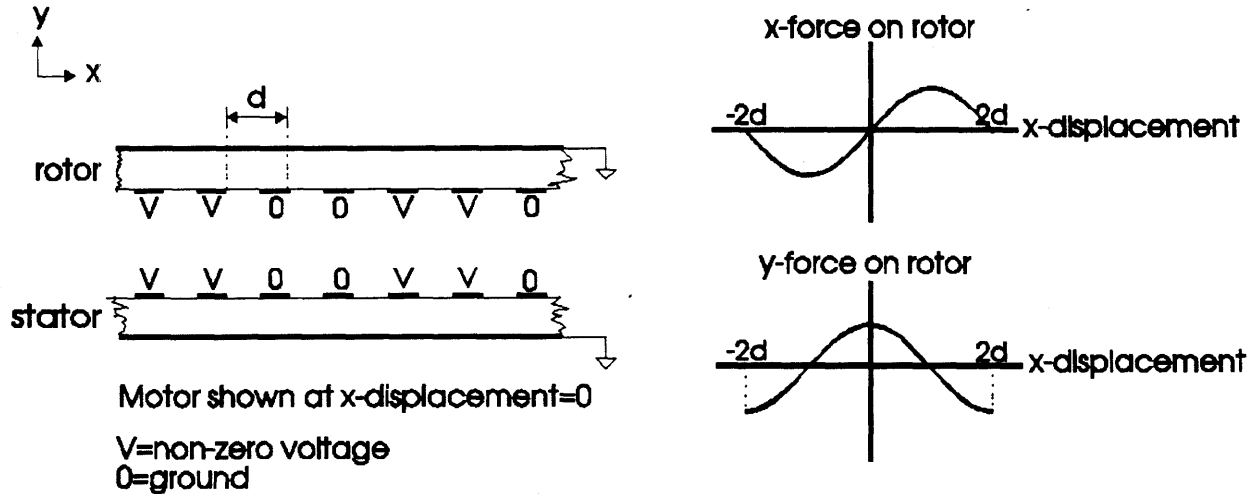
Figure 2.3a: Example voltage pattern   Figure 2.3b: Rough sketch of corresponding electrostatic forces

By judiciously choosing the voltages on the motor phases, the forces on the rotor can be controlled. From Figure 2.3b we see that there is a region where the y-force is positive, repulsing the rotor away from the stator. This design feature is advantageous, because a repulsive force may prevent the rotor from sticking down onto the stator, as may happen in other micromotors where such control over the y-forces does not exist.

However, we also see from Figure 2.3b that when the y-force is repulsive, the x equilibrium position is unstable. Because of this, the motor must be controlled using a closed loop to stabilize the x-position while maintaining a repulsive out-of-plane force.

To estimate the forces, rough calculations were performed. To simplify the calculations, the voltages on the rotor and stator were assumed to be sinusoidal in space, with amplitudes of V_0. These calculations are worked out in Appendices A and B, and the results are shown below

$$max(F_y) = \frac{\pi^2 \varepsilon_0 V_0^2}{16d^2}\left(1 - \tanh^2\left(\frac{\pi g}{4d}\right)\right) \qquad (2-1)$$

$$max(F_x) = \frac{\pi^2 \varepsilon_0 V_0^2}{16d^2 \sinh\frac{\pi g}{2d}} \qquad (2-2)$$

where d= 1/4 spatial period (as shown in Figure 2.3b)

g= out-of-plane gap between rotor and stator

These force equations can be used to estimate the forces per area for a given motor size, voltage, and configuration. Typical force densities for the motor Taussig used (parameters given in Section 2.1.3) were estimated to be 1.9 N/m^2 out-of-plane and 1.46 N/m^2 in-plane. Typical force densities for the motor used in this thesis (parameters given in Section 3.1) were estimated to be roughly 4.2 N/m^2 out-of-plane and 0.8 N/m^2 in-plane for g=0.015" and for V_0=400 V.

Position-sensing

In order to perform closed-loop control, a feedback position signal is necessary. The position-sensing method outlined below was developed by Carl Taussig, and the testing of the method forms the core of the thesis. In this design, the motor drive electrodes perform double-duty. Not only are they used to actuate the motor, but they are also used to detect the rotor's position, since the rotor-stator capacitance is position-dependent. The capacitance can be detected by superimposing high-frequency, low-voltage signals (dither signals) onto the rotor and measuring how much of these signals gets capacitively coupled to the stator phases. For a four-phase motor, two frequencies are sufficient to uniquely distinguish rotor positions throughout translation in y and throughout one spatial period in x. In this situation, eight signals are produced, each signal indicating how much of each frequency is coupled into each stator phase.

Suppose the stator phases are labeled A, B, C, and D, and the two dither frequencies, f_1 and f_2, have been superimposed on the rotor electrodes as shown in Figure 2.4 below. Then define V_{xi} as the amplitude of the dither signal of frequency f_i measured from stator phase x. The eight "raw" position signals produced can be labeled V_{A1}, V_{A2}, V_{B1}, V_{B2}, V_{C1}, V_{C2}, V_{D1}, and V_{D2}. Taussig has shown that these eight signals can be combined to form two in-plane position error signals: a direct signal (E_d) and a quadrature signal (E_q).

$$E_d = (V_{A1} + V_{C2}) - (V_{A2} + V_{C1}) \qquad (2-3)$$

$$E_q = (V_{B2} + V_{D1}) - (V_{B1} + V_{D2}) \qquad (2-4)$$

When normalized, these two signals uniquely identify the in-plane position of the rotor within one

spatial period.
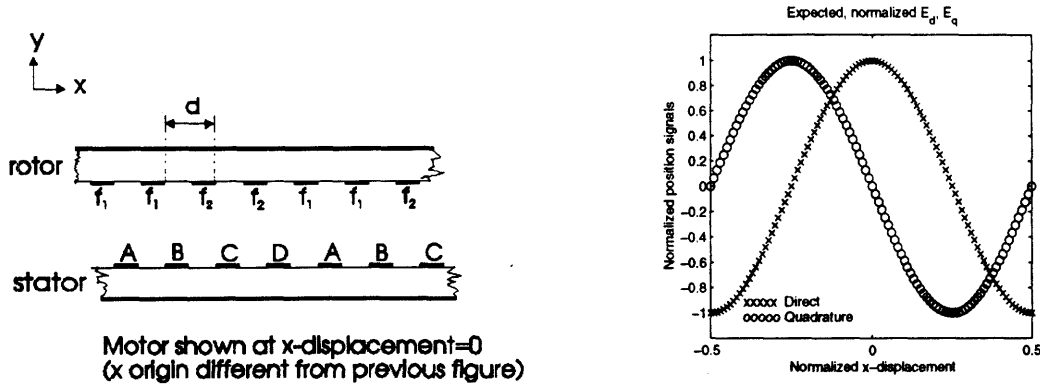
Figure 2.4: Normalized in-plane and quadrature position-error signals

To see how Equations 2-3 and 2-4 work, we need to look at the forms of the V_{xi} signals. For the setup of Figure 2.4, the V_{xi} signals can be approximately described as follows:

$$V_{A1} = A_{A1}\cos kx + B_{A1} \qquad V_{A2} = -A_{A2}\cos kx + B_{A2} \qquad (2-5a, b)$$

$$V_{C2} = A_{C2}\cos kx + B_{C2} \qquad V_{C1} = -A_{C1}\cos kx + B_{C1} \qquad (2-6a, b)$$

$$V_{B2} = -A_{B2}\sin kx + B_{B2} \qquad V_{B1} = A_{B1}\sin kx + B_{B1} \qquad (2-7a, b)$$

$$V_{D1} = -A_{D1}\sin kx + B_{D1} \qquad V_{D2} = A_{D2}\sin kx + B_{D2} \qquad (2-8a, b)$$

where π/k=2d in Figure 2.4

x=relative in-plane displacement between rotor and stator, as in Figure 2.4

A_{xi}, B_{xi}=constant coefficients

These equations only approximately describe the V_{xi} signals, which actually contain higher harmonics. Substituting Equations 2-5 through 2-8 into Equations 2-3 and 2-4 yields

$$E_d = (A_{A1} + A_{A2} + A_{C1} + A_{C2})\cos kx + [(B_{A1} + B_{C2}) - (B_{A2} + B_{C1})] \qquad (2-9)$$

$$E_q = -(A_{B1} + A_{B2} + A_{D1} + A_{D2})\sin kx + [(B_{B2} + B_{D1}) - (B_{B1} + B_{D2})] \qquad (2-10)$$

Figure 2.4 also shows the correspondence between normalized E_d and E_q signals and the rotor's position relative to the stator. The normalization factor used is

$$E_{norm} = \sqrt{E_d^2 + E_q^2} \qquad (2-11)$$

When scaled by E_{norm}, the direct and quadrature signals are independent of rotor-stator gap under normal motor operation. This normalization factor works under the assumption that E_d and E_q have roughly the same magnitudes (the A_{xi} are roughly equal and the B_{xi} are roughly equal) and on the assumption that E_d and E_q are harmonically pure (well modeled by sin waves). E_d/E_{norm} and E_q/E_{norm} are the actual in-plane position signals, not E_d and E_q alone. The normalized signals are independent of gap up to a point. If the gap were very large, these signals would not provide useful position information. However, the motor would not work in this case.

The eight V_{xi} signals can also be used to calculate a gap width signal that is independent of the in-plane position. A gap-width signal, E_{gap}, is obtained by summing the eight initial V_{xi} signals, creating an overall "parallel-plate" capacitance measurement which is inversely proportional to gap.

$$E_{gap} = V_{A1} + V_{A2} + V_{B1} + V_{B2} + V_{C1} + V_{C2} + V_{D1} + V_{D2} \qquad (2-12)$$

Going back to the example, if V_{xi} are given by Equations 2-5 through 2-8, the E_{gap} signal will be

$$E_{gap} = (A_{A1} - A_{A2} + A_{C2} - A_{C1})\cos kx + (A_{B1} - A_{B2} + A_{C2} - A_{C1})\sin kx + \sum B_{xi} \qquad (2-13)$$

Assuming that the A_{xi}'s are approximately equal, E_{gap} is approximately equal to the sum of the B_{xi} terms. In this way, the in-plane spatial information in the sinusoidal terms has been excluded.

The above method for finding in-plane position and gap width is not the only way; other schemes could involve using more dither frequencies and combining the raw signals in a different way in order to generate a sufficient position signal. However, the above method does minimize the number of high-frequency dither signals which must be superimposed onto the rotor, thus minimizing connections to the rotor. Also, this method provides robustness, because E_d/E_{norm} and E_q/E_{norm} are not dependent on the absolute magnitudes of V_{A1}, V_{A2}, etc., but on their differences. If V_{A1}, V_{A2}...V_{D2} were each multiplied by slightly different coefficients (for example $V_{A1}*1.02$, $V_{A2}*1.01$, $V_{C1}*0.99$, etc.), the form of the E_d and E_q signals in Equations 2-9 and 2-10

helps to average out these differences. This is also true for the E_{gap} signal. In addition, once E_d and E_q are divided by the normalizing factor, E_{norm} (Equation 2-11), the effect of the coefficients A_{xi} is further reduced, because they are divided out.

2.1.3 Preliminary experiments

To verify the concepts on which the design is based, Taussig performed several experiments using a dynamometer integrated with a mini-scale model of the electrostatic micromotor. This setup could measure the forces in the x- and y- directions between rotor and stator as a function of the xy position. The forces could be measured with a resolution of approximately 50 μN. In these experiments, the rotor and stator plates used were larger than those in the current project. The width of the electrode lines and spaces was approximately 0.010", and the rotor and stator plates were each 3.125" x 4.5". When the rotor-stator gap was approximately 0.02" and the applied voltage was 400 V, in-plane forces of +/- 5×10^{-3} N and out-of-plane forces of 3.5×10^{-3} to 8.0×10^{-3} N were measured. These force magnitudes are slightly smaller than expected from Equations 2-1 and 2-2, but they are in the right range. The experiments confirmed the shape of the force curves shown in Figure 2.4. Taussig also used the same setup to perform preliminary position-sensing tests. Oscilloscopes were used to extract the V_{xi} signals from the stator phases, successfully producing the position signals E_d/E_{norm} and E_q/E_{norm}. The gap signal was also successfully calculated from these signals. Finally, experiments were done to control the out-of-plane force independently of the in-plane force. This thesis has further confirmed the design by testing the position-sensing scheme on a milli-scale model of the motor using specially-designed electronics. All other electronics required for motor operation have also been designed and tested, however all of the electronics designed here could be much improved. Suggestions for improvements are given in Chapter 7.

2.2 Other related work

Several researchers have developed motors with similar design components, however, no one seems to have used the parts of the design together in the way described above.

2.2.1 DEMED linear motor

Niino, Higuchi, and Egawa have designed a motor which they have named DEMED (Dual Excitation Multiphase Electrostatic Drive) [4]. This motor is also a linear motor with a similar rotor and stator. It is also actuated by applying varying voltages to the rotor and stator phases. In addition, the "dual excitation" means that the DEMED also displays forces in the out-of-plane direction. So far, this motor sounds quite similar to Taussig's design. However, there are a few key differences. The DEMED makes no use of closed-loop control. It is driven instead by an open-loop AC power source. Therefore, it cannot take full advantage of the repulsive y-force. Also, having no closed-loop control, the DEMED does not use the rotor or stator phases as capacitive position sensors.

2.2.2 Closed-loop control for micromotors

Few people have tried to perform closed-loop control on micromotors. Researchers at Case Western Reserve University have developed a circuit, called the Micromotor Control Integrated Circuit (MCIC) [5], to perform closed-loop control for a rotational micromotor. However, their motor does not use repulsive out-of-plane forces, so their control system is different from one that would be needed to control Taussig's motor.

2.2.3 Capacitive position-sensing

Similar position-sensing schemes have been used in the past. In particular, the designers of the MCIC used the same technique of detecting in-plane position by sensing rotor/stator capacitance changes. Taussig's scheme detects position in two orthogonal directions, out-of-plane and in-plane, each independent of the other. Many other researchers have worked on capacitive position-sensing for micromotors. David Leip has done work on detecting very small micromotor capacitances in the presence of much larger parasitic capacitances. [6]

3.0 Experimental Motor

This chapter describes the specific motor implementation used in this thesis. The actual rotor and stator models and the mechanical mounts for them were designed and built by Carl Taussig. These are described in Sections 3.1 and 3.2.

3.1 Motor dimensions, materials, and electrical connections

The rotor and stator used here were made in the same manner as printed circuit boards. The insulating plate of each piece was made of Fr4 (a fiberglass composite with a dielectric permittivity of $4\varepsilon_0$), and the metal traces and ground plane for the stator were made of copper. The active surfaces of the rotor and stator are shown below in Figure 3.1.
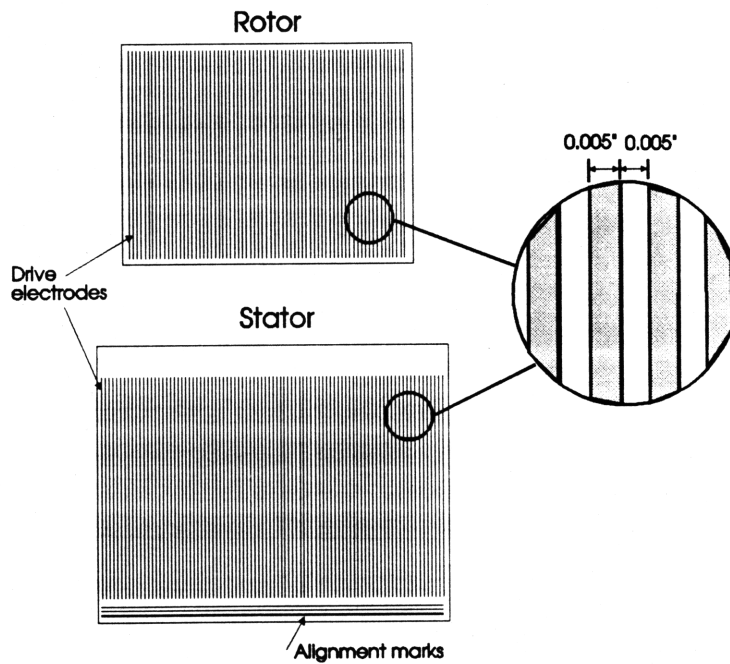
Figure 3.1: Rotor and Stator active surfaces

The drive electrode pattern covered an area of 2.1" x 2.8" on the rotor, and 2.2" x 3.35" on the stator. The electrode lines and spaces were 0.005" wide and are shown magnified in Figure 3.1. On the back side of the stator was a continuous metal ground plane. The total thicknesses (including metal traces) of the stator and rotor plates were 0.014" and 0.011", respectively. The alignment marks shown on the stator were also 0.005" wide lines and spaces. These were used for visually aligning the rotor to the stator. Typical rotor-stator gaps for the motor in this thesis

were about 0.01" to 0.015".

All electrodes with the same label are
electrically connected.
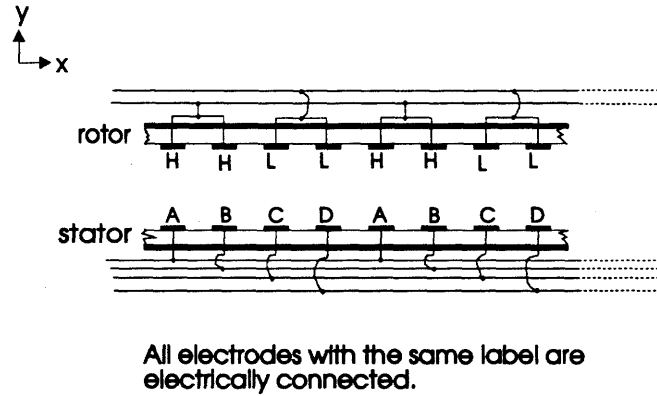
Figure 3.2: Electrical connections to rotor and stator

Figure 3.2 shows how the stator and rotor electrodes were electrically connected. All connections to individual electrodes were incorporated into the printed circuit design and were not hand-wired. The entire motor was designed to be four-phase, like the motor shown in Figure 2.2 and described in Chapter 2. Because the rotor was a moving part, the electrical connections to the rotor were made as simple as possible. For simplicity, it was decided that the rotor would have constant drive voltages (with super-imposed high-frequency, low-voltage signals for position-sensing), so that only the stator voltages would be actively controlled. The rotor voltage pattern shown in Figure 3.2 was chosen based on Taussig's previous work. This voltage pattern allowed the rotor to have only two electrically separate traces, one trace at high voltage (H) and one at low voltage (L). The stator's electrodes were grouped into four phases, also shown in Figure 3.2. Including the ground plane, the stator had five electrically separate traces.

This motor was smaller than the motor used in Taussig's previous experiments. The previous motor had 0.01" lines and spaces, twice as wide as those of the current motor. Also, Taussig's previous rotor and stator plates were larger in area and made using thicker insulating plates. Typical gaps for Taussig's motor were 0.02".

3.2 Motor mount

The mechanical mount for the rotor and stator was designed by Taussig and is shown in

Figure 3.3.
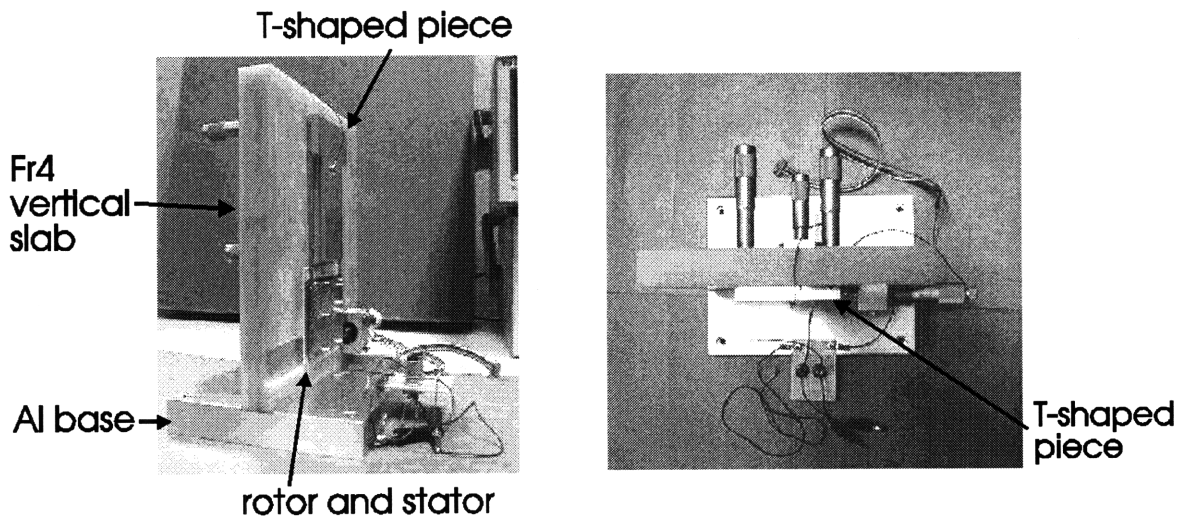
Figure 3.3: Motor mount: side view (left), overhead view (right)

The rotor and stator plates were mounted vertically, like two opposite walls of a room. Because of the vertical mount, the effect of gravity on the motor was like the effect on a pendulum. The stator was attached by adhesive to a thick vertical insulating slab of G-10 (9.15"x8"x1"), which rested on a heavy horizontal aluminum base (6"x8"x1"). The rotor was first attached to a light aluminum mounting frame by adhesive, then suspended from a T-shaped aluminum piece by two stainless steel leaf springs, designed to allow in-plane motion as shown in Figure 3.4. The springs were designed to be very flexible in the in-plane direction, so they would not exert much force on the motor--the primary external force on the rotor was gravity. In the first half of the project, 0.002" thick springs were used. However, these were so easily bent out of shape that it was difficult to align the rotor. Later, 0.004" thick springs were found to be superior. Their greater stiffness made it easier for the rotor to be positioned very close to the stator. The T-shaped aluminum piece was supported using a kinematic mount with four degrees of freedom controlled by micrometers. By positioning the T-shaped piece, the rotor could also be positioned. Additionally, a micrometer was

mounted to control the in-plane motion of the rotor and is shown in Figure 3.4.
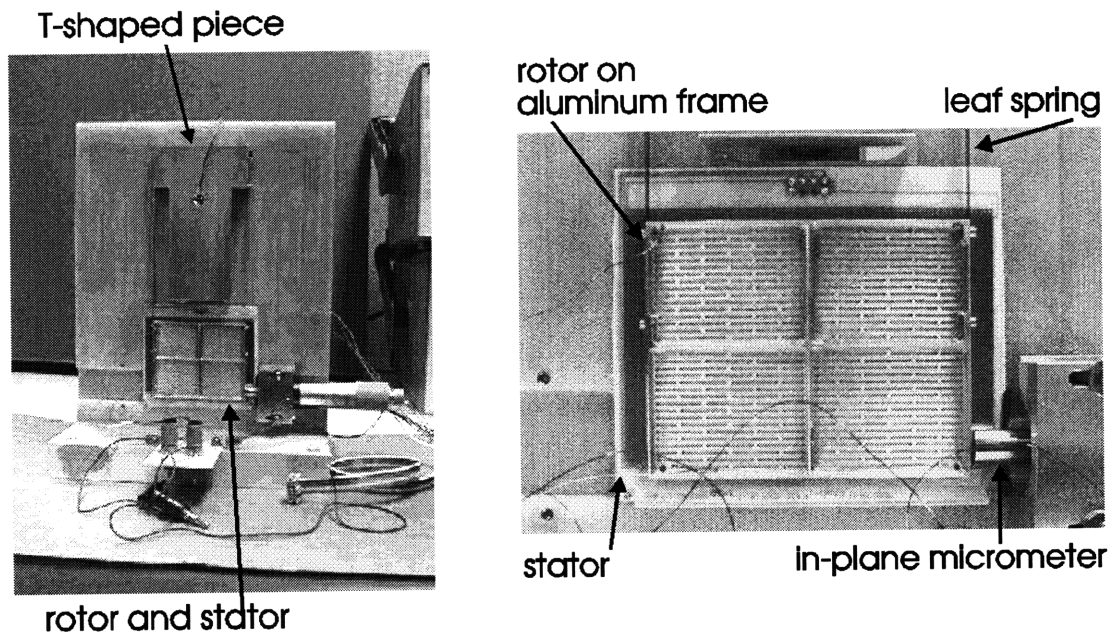
Figure 3.4: Front view of motor mount (left), Close-up of rotor/stator (right)

As mentioned above, the electrical connections to the rotor were minimized to reduce unnecessary mechanical influences. Two thin, 0.008" diameter wires were connected to the rotor and fastened to the heavy base for strain relief. The wires were allowed plenty of extra length to minimize their mechanical effect on the rotor. The rotor, its aluminum mounting frame, and the tape used to bind the rotor to the frame weighed 8.9 g.

Both the heavy metal base and the T-shaped aluminum piece were grounded. The aluminum frame, which was shorted to the T-shaped piece via the springs, thus formed the ground plane for the rotor. The entire setup was placed on a regular tabletop.

3.3 Rotor alignment

It was important for the rotor to be positioned parallel to the stator so that 1) the two plates were parallel to each other with a uniform gap and 2) the electrodes on those plates were parallel. A small rotor-stator gap was desirable, because it would increase the rotor-stator capacitances, producing greater forces and larger position signals. However, contact between the rotor and stator was undesirable because it would cause mechanical friction and electrical shorting. The rotor was positioned using micrometers to control the kinematic mount described above.

Two methods were used to gauge the uniformity of the rotor-stator gap: 1) visual inspection by shining a light through the gap and observing how much light emerged from the slit and 2) observing the amount of mechanical damping caused by friction between the plates (any observable damping indicated contact between the plates). Using these two methods, the rotor was brought as close and as parallel to the stator as possible without touching it. The micrometers were then adjusted by a known amount to change the gap. After the gap was made as uniform as possible, the lower edge of the rotor was aligned to the visual alignment marks shown in Figure 3.1. This ensured that the rotor and stator electrodes were parallel.

The shape of the rotor and stator plates affected the alignment. Ideally, the rotor and stator planes would have been perfectly flat. Initially, there were some problems, because both the rotor and stator were actually slightly concave. This happened because the glue (photo mount spray adhesive) holding the rotor and stator to their mounts was not strong enough, so the edges peeled away slightly. The peeling was most noticeable along the upper and lower edges of the stator and rotor. Because of this warping, the perimeters of the rotor and stator were closer together than the centers. This restricted how close the rotor and stator could be aligned without touching. However, later the rotor and stator were both remounted using doubled-sided masking tape, which improved the flatness. The glue probably didn't work because it was too old, not because the type of glue was inherently weak. Taussig had previously used the glue successfully on an earlier generation of the motor model. In addition, the aluminum frame that the rotor was mounted on was not perfectly flat, also affecting the rotor flatness.

3.4 Measuring the rotor-stator gap

Since the rotor and stator were not perfectly aligned, no single number could represent the gap, which varied across the plane. Also, in this motor setup, there was no good way of finding an absolute average gap measurement. The absolute gap was roughly estimated by sliding a piece of shim stock of known thickness into the gap without disturbing the rotor. Using this method, the smallest gap achieved without contact was roughly 0.005". However, this method only estimated the gap around the upper and lower edges of the rotor. During initial experiments, when both rotor and stator were concave, the center gap was roughly 0.012", even though the gap around the perimeter was around 0.005". Later, when a flatter rotor and stator were achieved, the overall gap was more uniform.

Although the absolute gap could not be measured accurately, the relative gap was easily measured. The gap measurements that follow refer to a relative gap setting, using an initial gap position as a reference. Because the stator was fixed, measuring the relative gap was equivalent to measuring the rotor position. As mentioned earlier, gap settings could be dialed into the micrometers of the rotor mount. To test the accuracy of these dialed-in gap settings, a beam-interrupt device was used to measure the position of the rotor. Figure 3.5 shows the setup of the device.
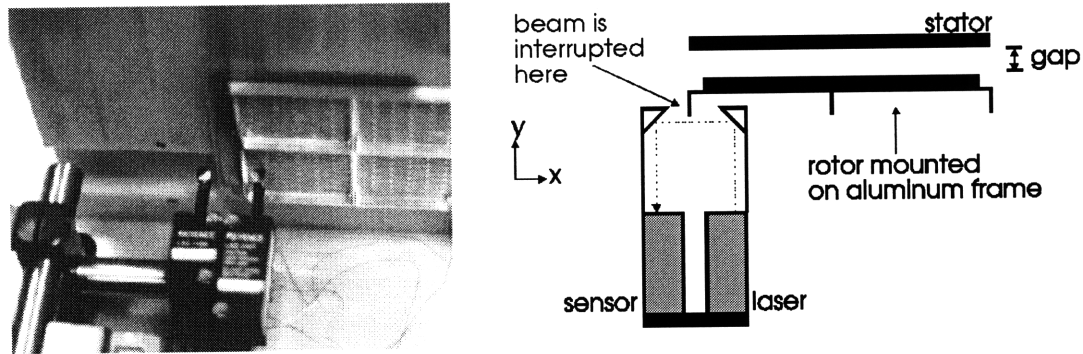
Figure 3.5: Beam-interrupt device setup

The device worked by emitting a laser beam, then measuring how much of this beam was interrupted by an object in its path. The change in the beam's area corresponded to a change in position of the object. In this case, the beam was interrupted by a piece of metal on the rotor's aluminum frame. This metal piece was orthogonal to the beam and to the plane of the rotor, as shown in Figure 3.5. The dotted line in the figure represents the laser beam. As the gap increased, the rotor moved out-of-plane, and more of the beam was blocked. Using this beam-interrupt device, an experiment was performed to test the accuracy of the dialed-in gap settings. During this experiment, the rotor was allowed to hang freely from the springs, without touching any other object. The dialed-in gap settings were changed and the change in rotor position was

measured using the beam-interrupt device. The results are shown in Figure 3.6

Accuracy of gap–control micrometers

Figure 3.6: Rotor's actual out-of-plane position compared to dialed-in setting

The two measurements should have yielded the same results, leading to a unity slope in Figure 3.6. However, Figure 3.6 shows that the beam-interrupt measurements were sm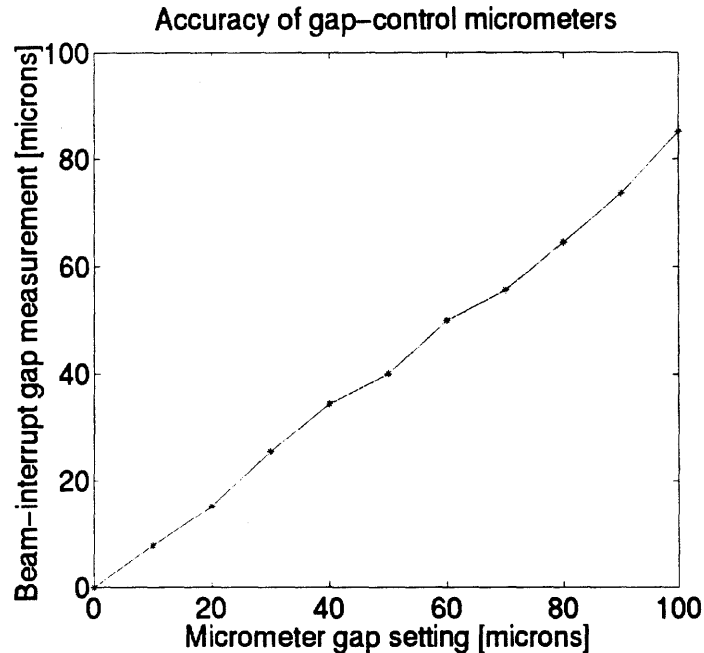aller than expected from the dialed-in settings. One reason for the discrepancy may be that the beam-interrupt device was not calibrated properly. Also, the rotor was connected to the micrometers by thin leaf springs which were not perfectly rigid, and the rotor's position may not have exactly copied the micrometer adjustments.

3.5 High-voltage tests

Although no high-voltage actuation experiments were conducted during this thesis, initial high-voltage tests were performed to make sure the motor parts could withstand the high voltages necessary to move them.

The rotor and stator were tested separately. To test the rotor, one trace pattern was grounded, while the other pattern was slowly raised to 475 V using a high-voltage power supply. The power supply was used in its constant current mode, with the current limit set as low as possible (10 mA). The stator was tested in a similar fashion: four of the five stator conductors were grounded while the remaining conductor (either an electrode pattern or the ground plane)

was slowly raised to 475 V. This was repeated for all five separate conductors on the stator. Figure 3.7a shows the initial test setup.
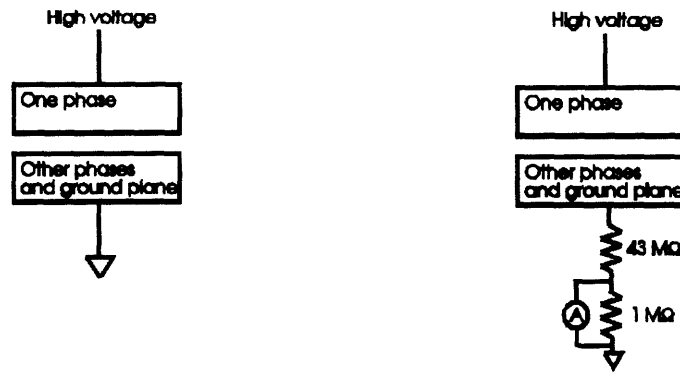

Figure 3.7a: Initial high-voltage test   Figure 3.7b: Revised high-voltage test

In these tests, several stator boards were destroyed when shorting occurred between the drive electrodes. The shorting usually occurred around 200-300 V. Figure 3.8 shows a close-up of the damage to one of the stator boards. The area shown in the figure is roughly 0.020"x0.025". The traces near the short had evaporated or melted away! It is likely that the power supply was not able to limit the current quickly enough, so the damage occurred.

These failures suggested that the stator and rotor might have been dirty. Both the stator and rotor were then cleaned in an ultrasonic acetone bath for about fifteen minutes and dried with compressed air. Then they were retested with a revised procedure, depicted in Figure 3.7b. A 43 $M\Omega$ + 1 $M\Omega$ resistor was placed in series to prevent further damage. The current was monitored with an ammeter as the voltage was slowly raised to 475 V. If shorting had occurred, there would have been a noticeable increase in current, but no such jump was observed. Both the stator and rotor passed this high-voltage test after they had been cleaned. Also, another test was run with only the 1 $M\Omega$ resistor in series. The rotor and stator were also able to withstand high voltages

under these conditions.

Figure 3.8: Close-up of melted traces on stator during high-voltage testing

All of these tests were performed on the rotor and stator when they were unmounted. Because of the particular mechanical setup, gaps less than 0.005" would be difficult to achieve without having some contact between rotor and stator. Smaller gaps (< 0.005") would be risky, because contact could easily occur if the setup were jostled, and because 400 V applied across 0.005" is already past the breakdown voltage of air ($\sim3\times10^6$ V/m). For 400 V, the distance at which breakdown occurs is 0.00525". In this thesis, the motor was not actually run at high voltages, but for high voltage operation, gaps should be kept around 0.01" or larger, to avoid air breakdown.

4.0 Position-sensing circuitry

4.1 Overview

Electronics were designed and built to implement the position-sensing method described earlier in Section 2.1.2. The electronics are shown as part of the system diagram in Figure 4.1. In
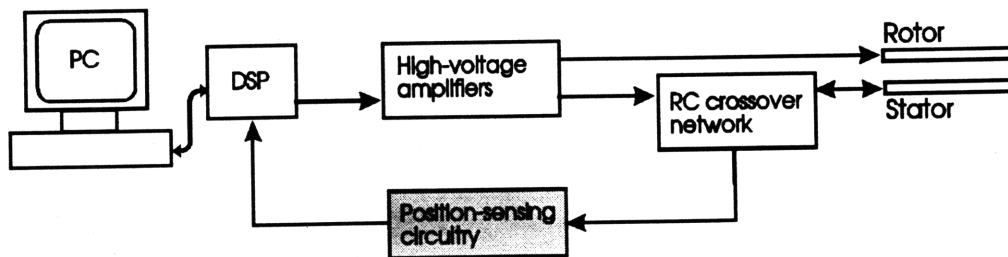
Figure 4.1: System block diagram; position-sensing circuitry shaded

this position-sensing method, the position information is encoded using AM modulation as the amplitude of a carrier (dither) wave. In order to use the E_d/E_{norm} and E_q/E_{norm} formulas (Equations 2-3, 2-4, 2-11), the V_{xi} signals must be found by demodulating the raw stator output (V_x). One way to extract the V_{xi} signals is depicted in Figure 4.2.
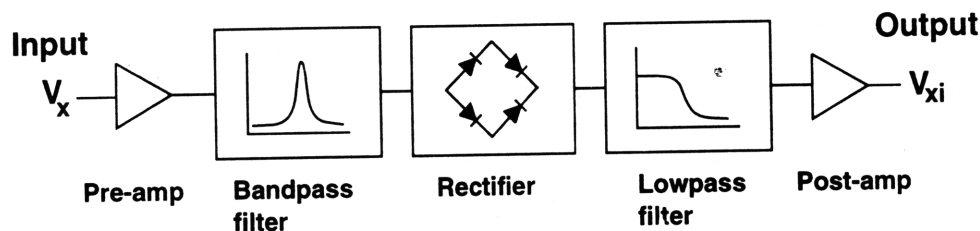
Figure 4.2: Demodulation scheme

In Figure 4.2, one demodulation channel is shown. Since the motor had four stator phases, each of which had to be demodulated for two frequencies, a total of eight demodulation channels were needed, one for each V_{xi} signal (x=A,B,C, or D; i=1 or 2). Four channels were designed to handle one dither frequency, and the other four channels handled the remaining dither frequency. These were assembled on a protoboard using Wire-Wrap. The schematic diagrams for the demodulation circuitry are shown in Appendix C.

Section 4.2 describes how the dither frequencies were chosen. Sections 4.3, 4.4, and 4.5,

discuss the bandpass filter, rectifier, and lowpass filter respectively. Finally, Section 4.6 evaluates the overall demodulator performance.

4.2 Choosing dither frequencies

Three criteria were used to choose the two dither frequencies:

1) the frequencies had to be high enough to resolve the motor's motion in time,

2) the frequencies had to be sufficiently far apart so that the bandpass filter could distinguish them, and

3) the bandpass filter and other demodulators components had to be able to work at those frequencies.

The DSP that would perform the control algorithm was capable of sampling the position information at up to 10 kHz. Following a rule of thumb for a noise-limited digital servo, the control loop was estimated to have bandwidth around 1 kHz, and the motor's motion would fall within this bandwidth. Since the dither frequencies control the time-resolution of the position signal, they had to be much higher than 10 kHz, the sampling rate. The higher the dither frequencies, the greater the time-resolution of the signal.

However, the choice of dither frequency was also limited by the decision to use switched-capacitor bandpass filters in the first stage. The best filter readily available had a maximum center frequency around 100 kHz while maintaining a $Q\sim20$.

Finally, if the dither frequencies were too close together, the bandpass filters would not be able to select a single frequency--information about both frequencies would overlap into all demodulation channels.

Based on these criteria, dither frequencies $f_1=70$ kHz and $f_2=95$ kHz were chosen. In addition, these were close to the frequencies used by Taussig in his initial, successful experiments with this position-sensing technique.

4.3 Bandpass filter

4.3.1 Design criteria

The ideal bandpass filter for this application would have had a perfectly flat passband, centered about one of the dither frequencies. More design criteria can be uncovered by examining

a hypothetical input to the bandpass filter:

$$V_x(t) = \frac{A}{2}[1 + M\sin(\omega_m t)]\sin(\omega_{c1} t) + \frac{A}{2}[1 + M\cos(\omega_m t)]\sin(\omega_{c2} t) \qquad (4-1)$$

$$= \frac{A}{2}\left[\sin(\omega_{c1} t) + \frac{M}{2}\cos(\omega_{c1} - \omega_m)t - \frac{M}{2}\cos(\omega_{c1} + \omega_m)t\right]$$

$$+\frac{A}{2}\left[\sin(\omega_{c2} t) + \frac{M}{2}\sin(\omega_{c2} - \omega_m)t + \frac{M}{2}\sin(\omega_{c2} + \omega_m)t\right]$$

where V_x=signal from single stator phase x

ω_{ci}=dither frequencies ($\omega_{ci}/2\pi \sim$ 70-100 kHz)

i=dither frequency index (i=1 or 2)

ω_m=modulation envelope (position signal) frequency ($\omega_m/2\pi <$ 1 kHz)

A=amplitude

M=percent modulation ($0 \le M \le 1$, corresponding to a range of 0% to 100%)

Suppose we want to pass the terms dealing with dither frequency 1. The bandpass filter must have a wide enough passband to pass $\cos(\omega_{c1} +/- \omega_m)$, while still attenuating the signal components from the other dither frequency. However, since no filter will be perfectly flat, it is also important for the bandpass filter to be symmetrical about the center frequency. A fast transient response is also desirable. Since the design is for a maximum modulation frequency of 1 kHz, the maximum motor speed the circuit can handle is (1 kHz)(0.040")~1 m/s. If the motor were to move faster than 1 m/s, the motion would be beyond the bandwidth of the circuit.

4.3.2 Bandpass implementation: LMF100

Initially, a Sallen-Key design was investigated for the bandpass filter, but a switched-capacitor filter was later chosen because of time constraints on the thesis. The advantages of a switched-capacitor filter are that the bandpass center frequency can be easily changed by altering the clock frequency, and that the filter is easy to use. However, this type of filter does have clock noise which would not exist in a Sallen-Key design. [7] Many types of switched-capacitor filters were reviewed, but the LMF100 was chosen because it could realize filters with high center frequencies (~100 kHz) and relatively high Q's compared with other switched-capacitor filters. In general, a high Q was desired, because the higher the Q, the more the bandpass filter would be able

to selectively pass a single dither frequency with minimal overlap from the neighboring dither signal. However, if the passband region were too narrow ($< 2\omega_m$), the gain at frequencies ω_{ci} +/- ω_m might be too low.

4.3.3 Type of filter: Butterworth

Once the LMF100 was chosen and passed preliminary tests, the type of bandpass filter was chosen. The LMF100 is capable of implementing Butterworth, Chebyshev, Bessel, and other classical filters. Although a Chebyshev filter was considered, the Butterworth design was used because it was simpler to implement and did not have passband ripples (which might distort the modulation envelope). Although the Butterworth filter had a slower time-domain response than the Chebyshev, it was still faster than the Bessel filter and so provided a compromise between the Chebyshev and Bessel. The bandpass filter is shown below as it was used during experiments.
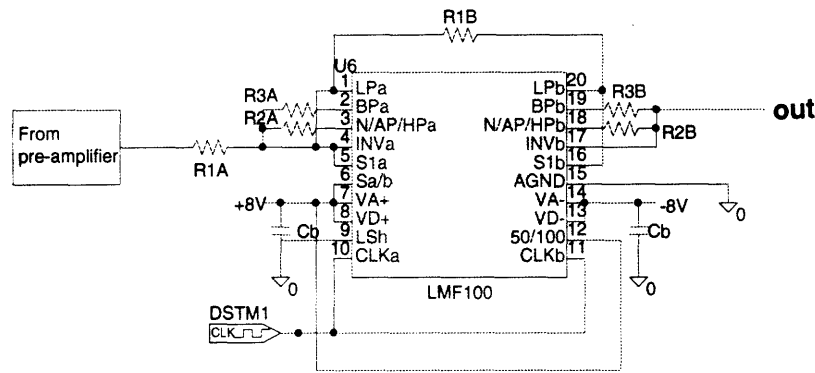
Figure 4.3: Bandpass filter: implemented circuit

The LMF100 was used in mode 1b to create two cascaded 2nd-order Butterworth bandpass filters having the following total transfer function:

$$H(s) = \left| \frac{\left(\frac{-R_{3a}}{R_{1a}}\right)\left(\frac{\omega_{0i}}{Q_a}\right)s}{s^2 + \left(\frac{\omega_{0i}}{Q_a}\right)s + \omega_{0i}^2} \right| \left| \frac{\left(\frac{-R_{3b}}{R_{1b}}\right)\left(\frac{\omega_{0i}}{Q_b}\right)s}{s^2 + \left(\frac{\omega_{0i}}{Q_b}\right)s + \omega_{0i}^2} \right| \qquad (4-2)$$

$$\omega_{0i} = 2\pi f_{0i} = 2\pi f_{CLK\_i}\left(\frac{\sqrt{2}}{50}\right) \qquad (4-3)$$

$$Q_{a,b} = \frac{f_{0i}}{(\text{-3 dB bandwidth of output})} = \frac{R_{3(a,b)}}{R_{2(a,b)}}\sqrt{2} \qquad (4-4)$$

where R_{1a}, R_{2a}, R_{3a}=external resistors for 1st stage (2nd-order Butterworth filter)

R_{1b}, R_{2b}, R_{3b}=external resistors for 2nd stage (2nd-order Butterworth filter)

Q_a=Quality factor for 1st filter stage

Q_b=Quality factor for 2nd filter stage

$\omega_{0i}=2\pi f_{0i}$=bandpass center frequency (same for both stages)

f_{clk_i}=clock frequency input to LMF100 (same for both stages)

i=dither frequency index

This filter could have been improved. It was later realized that the LMF100 could have been used in mode 3, which would have allowed two internal clock signals to be created from one external clock signal, using a few additional external components. However, this option was not pursued at the time of design. Using mode 3 would have been better, because it would have easily allowed a 4th-order Butterworth filter to be implemented without extra equipment. A 4th-order filter would have had a flatter passband and steeper transition region. However, since the Butterworth filter has a maximally flat passband in any case, this improvement may not be significant.

4.3.4 Clock and dither signal sources

Including the two dither signals (ω_{ci}) and two LMF100 clock signals (f_{clk_i}), four separate periodic signals had to be generated. However, only two signal generators were required to produce all four signals. This was possible because each clock frequency is related to its corresponding bandpass center frequency by a factor of ~35.4 (Equation 4-3). To take advantage of this, an Altera EPLD (Erasable Programmable Logic Device) was programmed to perform a divide-by-35.3 function. If the EPLD received an input square-wave of frequency f, it would output two square-waves at frequencies: f/212 and f/6. The program for the EPLD was written by

Carl Taussig and is listed in Appendix D. Two such EPLD's were used, one for each dither frequency. In summary, two signal generators fed a high frequency signal to two EPLD's, each of which produced a dither and clock signal. The signals produced by the EPLD's were square waves.

Problems with the clock and dither signal sources

Ideally, the dither signal frequency (ω_{ci}) and bandpass center frequency (ω_{0i}) should have been exactly the same. In reality, there were several issues involving the clock signals which affected the bandpass center frequency. These problems suggest the dangers of having a passband that is too narrow--it is too difficult to align the bandpass center frequency and dither frequency.

First, since 212/6~35.3, this was an approximation to 35.4 and would result in some error: the dither signal frequency and bandpass center frequency might not be the same.

Second, it was also found that the dither frequency and bandpass center frequency might differ by several kHz, depending on the external components to the LMF100. These components were chosen to minimize the difference between the dither frequency generated by the EPLD and the center of the bandpass.

Third, the f_{clk_i}/f_{0i} ratio shown in Equation 4-3 was slightly different, depending on f_{clk_i}. In the LMF100 data sheets, a graph is given showing the ratio's dependence. In early experiments, it was determined that for f_{02}=95 kHz, it would be better to use a ratio of 36 instead of 35.3, which agreed with the information in the LMF100 data sheet, which is shown in Appendix E. However, later in the thesis, measurements were taken which showed that a ratio of 35.3 was better for producing a bandpass center frequency of 95 kHz. This issue remains unresolved.

Fourth, although each chip was slightly different, with a slightly different f_{clk}/f_{0i} ratio, all four 70 kHz LMF100 filters received the same f_{clk_1}, and all four 95 kHz filters received f_{clk_2}. This was another reason that the bandpass center frequencies were not precisely aligned to the dither frequencies.

The above difficulties show why it is dangerous to have a bandpass filter with too narrow a passband. It is difficult to precisely place each filter's f_{0i} exactly at the same frequency as the corresponding dither signal. A narrow passband which is not at the exactly same frequency as the dither signal may miss the signal entirely and attenuate it instead.

4.3.5 Filter parameters and performance

After some experimentation, the following values were chosen to yield two cascaded 2nd-order filters, each with a Q of 10. The overall passband gain was 1 dB and overall Q was about 17. The components in Table 1 refer to Figure 4.2 and Equations 4-2 through 4-4.

Table 1: Component values for LMF100 bandpass filter

Component Name	f_c [kHz]	Resistance [kΩ]
R_{1a}	70	34.8
R_{1a}	95	42.2
R_{1b}	70; 95	50 (variable)
R_{2a}	70; 95	8.25
R_{2b}	70; 95	8.25
R_{3a}	70; 95	61.9
R_{3b}	70; 95	61.9

In initial experiments, it was found that when the same filter IC was operated at different clock frequencies (all other parameters held constant), different gains resulted. For this reason, the R_{1a} resistors had different values, depending on f_c. A variable resistor was used for R_{1b} to adjust for differences between chips. Figure 4.4 below shows the experimentally measured transfer functions for two different bandpass filters, one with f_{c1}=67 kHz, and one with f_{c2}=95 kHz. 67 kHz was used instead of 70 kHz because of a restriction on f_{clk_1} due to equipment. R_{1b}= 39.4 kΩ was used for the filter at f_{c1}=67 kHz, and R_{1b} = 35.0 kΩ was used for the filter at f_{c2}=95 kHz. Using these components, the expected transfer functions from Equations 4-2 through 4-4 were
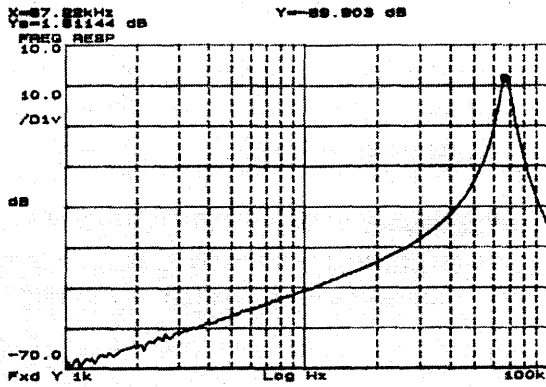
calculated and are shown in Figure 4.5.

Figure 4.4a: Experimental bandpass transfer function with f_c=67 kHz
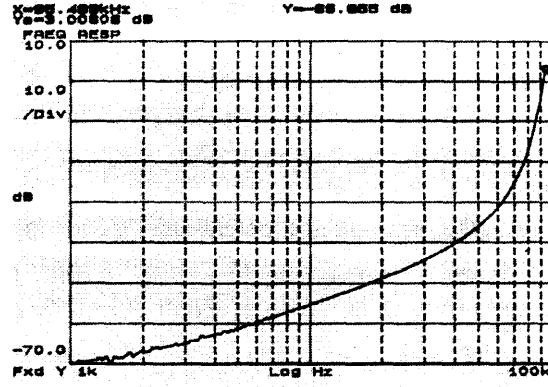
Figure 4.4b: Experimental bandpass transfer function with f_c=95 kHz
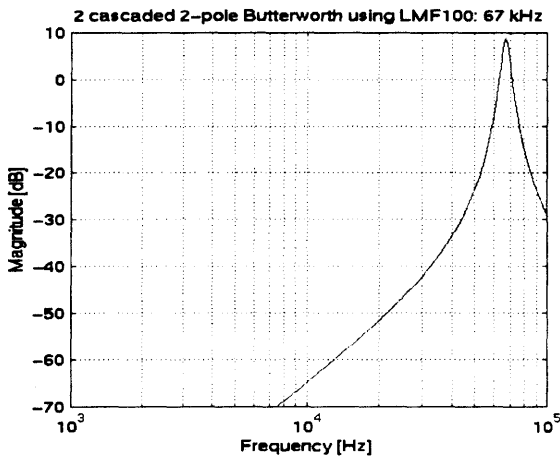
Figure 4.5a: Expected bandpass transfer function with f_c=67 kHz
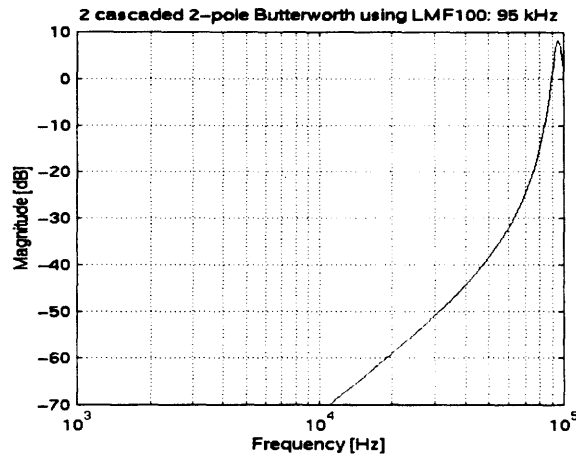
Figure 4.5b: Expected bandpass transfer function with f_c=95 kHz

As can be seen from the figures, experimental gain and peak sharpness were lower than expected. For both experimental filters, the peak gain was roughly 5 dB greater than the gain at the non-peak dither frequency.

Figure 4.6 shows close-ups of the passband peaks for the experimental filters. (Note that the horizontal axes are on different scales.) Unfortunately, these passband regions were not very

flat. For both filters, the passband is only flat for about 2 kHz.

Figure 4.6a: Experimental bandpass peak
with f_c=67 kHz

Figure 4.6b: Experimental bandpass peak
with f_c=95 kHz

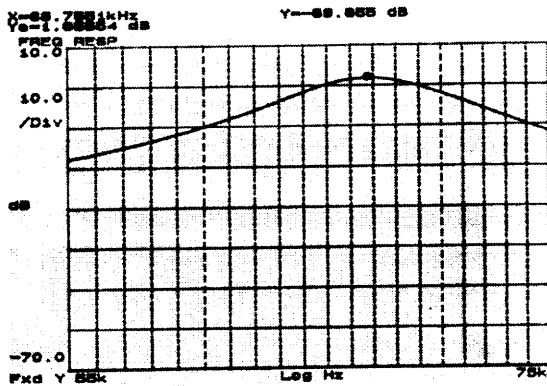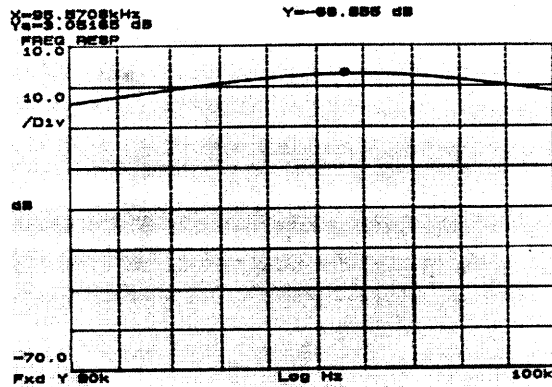In future, a 4th-order filter should be implemented in mode 3, because only a few more external components would be needed to implement it, and it would improve performance. Using a 4th-order Butterworth filter would increase the passband flatness and transition-region steepness slightly, coming closer to the ideal filter. From Figure 4.5, the cascaded 2nd order filters yield a 3 dB passband of roughly 4 kHz.

Finally, offset voltage was another important element of the bandpass filter. Ideally, the output of the bandpass filter would have no DC component, however, in reality the output was offset by around -0.1 V. This output offset was independent of the input offset or input amplitude. Since the signal range was expected to have an amplitude of around 2 V, the offset from the bandpass filter was not expected to cause problems.

4.4 Absolute value circuit: implemented using multiplier

Initially, a standard full-wave rectifier, using three diodes and an op-amp, was considered. However, for convenience, a multiplier IC (AD734) was used instead, shown below in Figure 4.6. Using the multiplier, the function X^2/D was implemented. Although this was not an absolute value function, it did ensure that the signal became positive, so that the position signal would be preserved after going through the lowpass filter. The value of the denominator, D, was controlled by external resistors. The multiplier chip was tested by feeding it a +/- 4V square wave, which was transformed into a single DC voltage ~7V. Thus, the experimental value of D was ~2.8, which was close to the expected value of D=3 that the external resistors had been chosen to create. D was

maintained at this value through the rest of the project. There were some periodic spikes in the output, but for the most part it performed adequately. This experiment was tried at various frequencies (5 kHz, 100 kHz) and seemed to work just as well at either frequency.
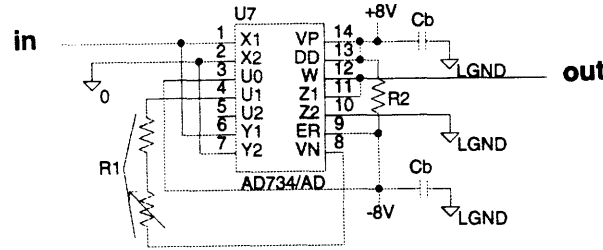
Figure 4.7: Multiplier circuit diagram

4.5 Lowpass filter

The criteria for the lowpass filter were less stringent than those for the bandpass filter. The lowpass filter needed to preserve low-frequency (< 5 kHz) signals while attenuating the high-frequency dither signals (70-95 kHz). However, it was also important for the passband to be flat in the region where the position signal would be expected (< 1 kHz).

A switched-capacitor filter was also used to implement the lowpass filter. The LMF40, a 4th-order Butterworth lowpass filter, was chosen for ease of use. An advantage of this IC was that no external clock signal was needed to set the lowpass filter's cutoff frequency. Instead, external components could be used to set an internal clock frequency. There was no way to control the gain on the LMF40, so a standard non-inverting op-amp was placed after the lowpass filter in each demodulation channel to control the gain.

External components (R=2.61 kΩ, C=680 pF) were chosen to yield an expected cutoff frequency of 8.2 kHz, since the experimental cutoff frequency was found to be lower than

expected. Figure 4.8 shows a typical lowpass transfer function.
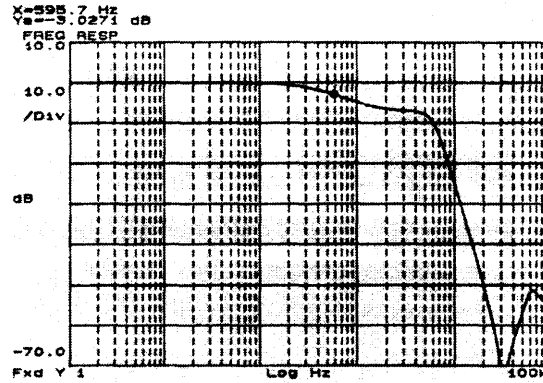
Figure 4.8: Experimental lowpass transfer function

This figure shows that the passband region is not flat. Around 200 Hz - 1100 Hz, there is a 5 dB dip before the main knee around 5 kHz. This is bad, because it means that the output amplitude depends on the frequency of the position signal, possibly distorting the position signal. In future, this might be improved by moving the cutoff frequency up by 15 or 20 kHz or by using a different kind of lowpass filter.

4.6 Overall demodulator performance

Despite the fact that the demodulator was not optimized, it still performed its basic function. A few experiments were performed on the overall demodulator to explore its characteristics. In particular, the dependence of the output on the input amplitude, frequency, and percent modulation were investigated. Also, frequency spectra were taken at various stages as a known signal passed through the demodulator, giving noise information.

Theoretically, if the input signal is as follows:

$$V_x(t) = \frac{V_{pp}}{2}[1 + M\sin(\omega_m t)]\sin(\omega_{c1} t) + \frac{V_{pp}}{2}[1 + M\cos(\omega_m t)]\sin(\omega_{c2} t) \qquad (4-5)$$

then the final demodulator output signal should be

$$V_{xi}(t) = \begin{cases} K\dfrac{V_{pp}^2}{4}\left[\dfrac{1}{2} + M\sin(\omega_{c1}t)\right] & \text{if } i=1 \\[4mm] K\dfrac{V_{pp}^2}{4}\left[\dfrac{1}{2} + M\cos(\omega_{c2}t)\right] & \text{if } i=2 \end{cases} \qquad (4-6)$$

where i=dither frequency index

x=stator phase index

K=constant gain (depends on gain of each stage)

V_{pp}=input amplitude

M=percent modulation ($0 \le M \le 1$, which corresponds to a range of 0% to 100%)

$\omega_{ci}=2\pi f_{ci}$=dither frequency (70-95 kHz)

$\omega_m=2\pi f_m$=modulation frequency (< 1 kHz)

The theoretical output (Equation 4-6) takes into account the X^2/D function, but assumes a perfect bandpass and perfect lowpass filter. In Equation 4-6, the value of i depends on which dither signal the demodulation channel is tuned for, f_1 or f_2. Experimentally, the output was different from Equation 4-6 because of noise, saturation at various stages, and imperfect filters. In addition, Equation 4-5 only represents a hypothetical input, with a sinusoidal modulation and sinusoidal dither signal.

4.6.1 Varying the input amplitude

In this experiment, an unmodulated (M=0) 95 kHz square wave with no offset was fed to the demodulator, producing a DC value at the output. A square wave was chosen, because the dither signals produced by the Altera EPLD were square waves. The output level was observed as the input peak-to-peak amplitude ($V_{pp}=V_{max}-V_{min}$) was varied. From Equations 4-5 and 4-6, we would expect a graph of the output level to input amplitude to resemble an V_{pp}^2 function. Figure

4.9 shows the relationship between input peak-to-peak amplitude and output level.
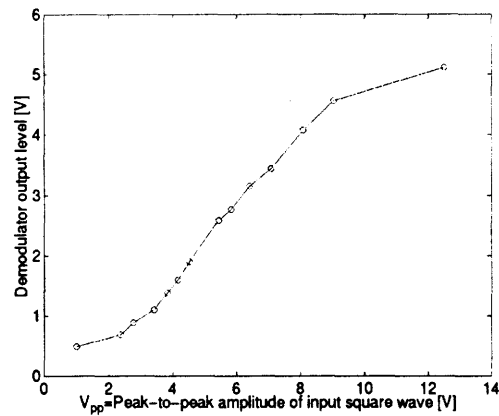
Figure 4.9 Varying the input amplitude to the demodulator

When the peak-to-peak input amplitude nears 10 V, the output starts leveling off. This was probably due to saturation of the signal at some stage of the demodulator, most likely the multiplier. Each stage was powered by +/- 8V power supplies and could only handle signals within this range. For example, when an input signal with V_{pp}=10 V passes through the multiplier, the maximum predicted voltage is roughly $5^2/2.8 \sim 8.9$ V. This is higher than the multiplier can handle, so it saturates, and the signal is deformed.

4.6.2 Varying the input modulation frequency

Ideally, the output should not depend on the input modulation frequency, as long as this frequency is within a reasonable range (< 5 kHz). In this experiment, the input modulation frequency (ω_m) was changed while all other input parameters were held constant. Referring back to Equation 4-5, the input signal was a modulated 98 kHz sine wave with M~1, V_{pp}=8 V. The following graph shows the dependence of the output amplitude on the input modulation

frequency.

Figure 4.10: Varying the input modulation frequency to the demodulator

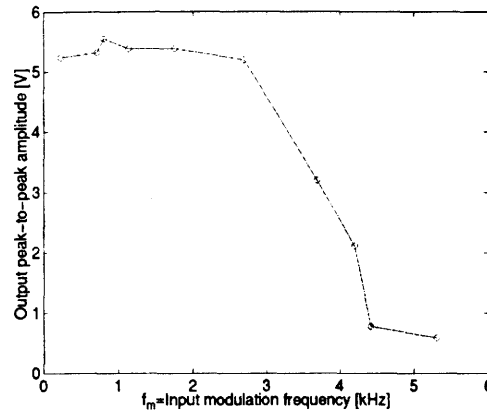The output amplitude stays roughly constant around 5.4 V for frequencies between 0.2 kHz and 2.8 kHz. This is lower than the expected output of about 7.16 V, but it is possible that the lowpass stage or post-amp may have attenuated the signal slightly; the individual lowpass gain was not measured in this experiment. After 2.8 kHz, the output amplitude decreases sharply for frequencies above 2.9 kHz. It is possible that the dependence of the output on the input modulation frequency is due to the lowpass filter. However, according to Figure 4.8, the lowpass filter's sharp drop occurs between 4-5 kHz, not around 3 kHz. This experiment was done on a demodulation channel containing a different lowpass filter than the one whose transfer function is shown in Figure 4.8, which may explain why the lowpass transfer function and Figure 4.10 do not match. So it is still possible that the curve in Figure 4.10 could be explained by the lowpass filter. The shape of Figure 4.10 is probably not due to the multiplier, which has a bandwidth in the MHz range.

In any case, further tests should be done on modulation frequencies between 0-1 kHz, since this is the expected range for the motion of the motor. It would be bad if the output amplitude varied significantly for frequencies less than 1 kHz, because the demodulator output might be distorted.

4.6.3 Varying the input percent modulation

In another experiment to test the demodulator, the input percent modulation (M in Equations 4-5 and 4-6) was varied while all other parameters except amplitude (V_{pp}) were held

constant. Two values were tried for M, 0.5 and 1. In both cases, the input signal was a 95 kHz square-wave modulated with a 1.7 kHz sine wave. The results of the test are shown in Figure 4.11.
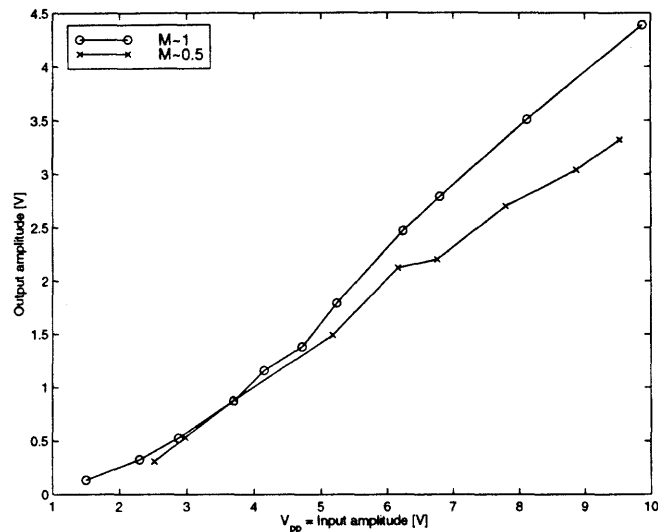
Figure 4.11: Varying the input amplitude and percent modulation to the demodulator

As expected from Equations 4-5 and 4-6, the output/input amplitude ratio is higher for higher values of M. At the time of this experiment, it was not known what percent modulation might be detectable when the motor was actually hooked up to the demodulation circuit. The lowest detectable percent modulation was limited by the amplitude of the noise introduced through the demodulator. Later it was found that percent demodulation values of M~0.1 - 0.2 were detectable if the motor was aligned well and hooked directly to the demodulator circuit.

4.6.4 Spectra at various stages

To get some idea of the noise present in the demodulator, a frequency spectrum of a known input signal was measured at various stages as the signal traveled through the demodulator. An input 70 kHz sine wave was modulated by a 0.8 kHz sine wave. The resulting spectra are shown in Figures 4.12-4.15. The spectra on the left of each figure range from 0 Hz to 15 kHz, and the spectra on the right of each figure range from 0 Hz to 500 kHz. The vertical axes are on scales

of 10dB/division.

Figure 4.12: Output of pre-amp, input to bandpass filter
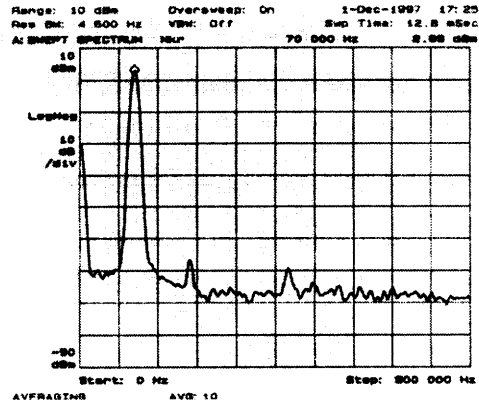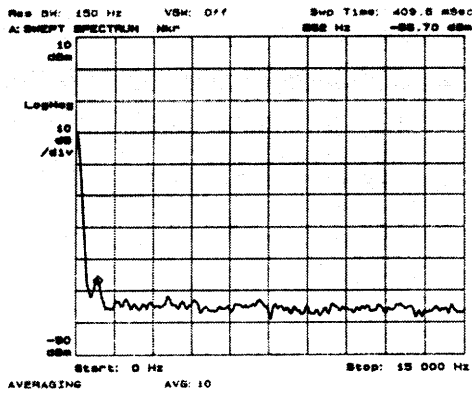
Figure 4.13: Output of bandpass filter, input to multiplier
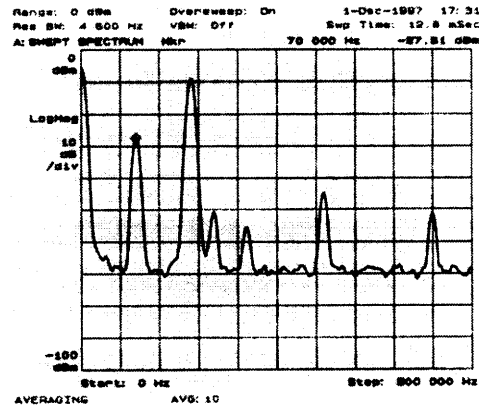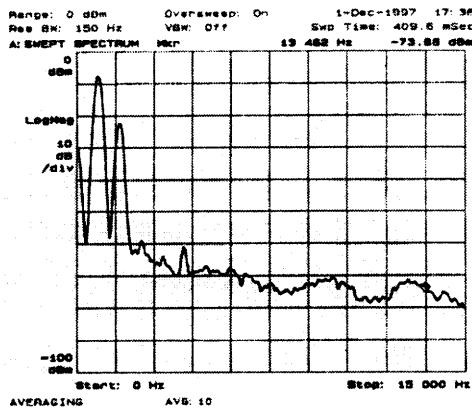
Figure 4.14: Output of multiplier, input to lowpass filter

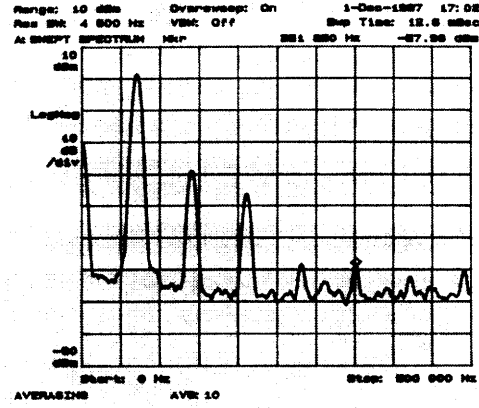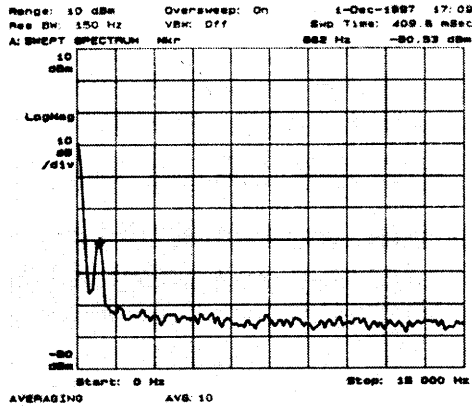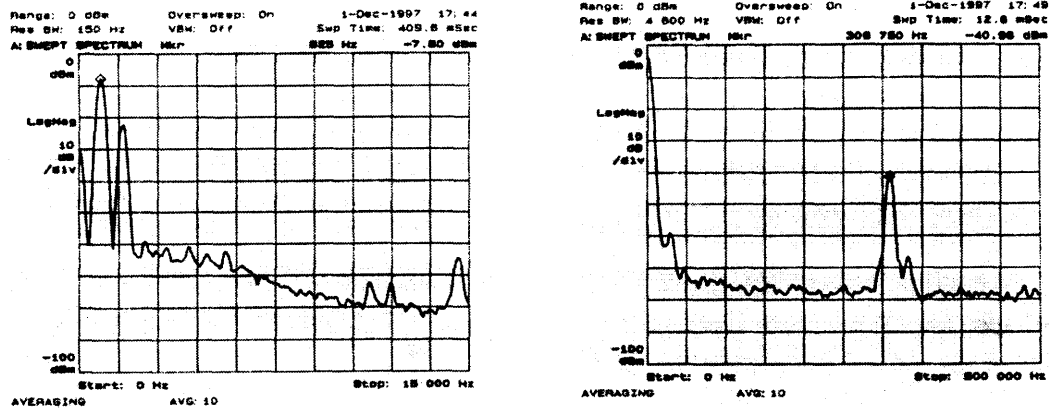Figure 4.15: Final output: Output of lowpass filter

The input signal in Figure 4.12 has peaks at 0.8 kHz, 70 kHz, and harmonics of 70 kHz as expected.

After the signal goes through the bandpass filter, Figure 4.13 results. The 70 kHz peak is about 60 dB above the noise. Next, the signal passes through the multiplier, where the carrier (dither) frequency gets doubled and higher frequencies are produced, as shown in Figure 4.14. In addition, the position information at 0.8 kHz is extracted.

Finally, Figure 4.15 shows the final output of the demodulator, the lowpass output. The main signal at 0.8 kHz is at least 30 dB above the clock noise of the lowpass filter which is around 300 kHz.

From these spectra we see that there is some noise contamination from the clock signal in the lowpass filter, but no overwhelming noise that competes directly with the signal level.

4.6.5 Summary of demodulator tests

In summary, the demodulator performed roughly as expected. In the input amplitude test, the shape of the curve was as expected. The modulation frequency test should have been performed with more data points between 0 kHz and 1 kHz, the actual region of interest over which the curve in Figure 4.10 should have been flat. The demodulator circuit could detect percent modulation values down to 0.1-0.2. However, it was not known what the actual percent modulation values were for the motor. Finally, spectra were taken at each stage of the demodulator to monitor noise.

4.7 Calibrating the position signal

After all eight demodulation channels were assembled and tested, the next step was to see if they would be able to extract a meaningful position signal when connected to the motor. For simplicity, this task was broken into three phases: 1) preliminary experiments getting position signals from the motor without using the demodulator circuit, 2) getting position signals with the demodulator hooked directly to the stator phases, and 3) getting position signals using the RC network as an interface between the stator phases and the demodulator. Phase 1 allowed the motor model and setup to be tested alone, without the added complications of the demodulator circuit. Once the mechanical setup was investigated, phase 2 allowed the demodulator circuit to be tested without involving the complications of the RC network. Unfortunately, phase 3 could not be completed in the given time. The RC network is important, because it is needed to protect the position-sensing circuitry while the motor is being driven by high (~400 V) voltages.

4.7.1 Preliminary experiments without the demodulator circuit

Many of the experiments here repeated Taussig's position-sensing experiments described in Section 2.1.3. Like Taussig's experiments, these involved using the FFT functions on oscilloscopes to perform the same functions the demodulator would to extract the position signal. Signal generators were used to create the 70.0 kHz and 95.1 kHz sine wave dither signals with peak-to-peak amplitude of V_{pp}~19.7 V, which were connected directly to the rotor electrodes. The stator phases were directly connected to oscilloscope channels. Two digital oscilloscopes were used, an HP54601A and an HP54602A, to perform the same function--an FFT. One oscilloscope was connected to stator phases A and C, and the other oscilloscope was connected to stator phases B and D. Each scope performed an FFT on each V_x signal. For each of the four FFTs, the peak heights at 70 kHz and 95 kHz were measured visually and recorded by hand. In this way, the eight "raw" V_{xi} position signals were measured. The rotor's position was controlled by the various micrometers described in Section 3.2. As the motor was moved, the position signals were recorded.

In-plane signals using oscilloscopes

As was described in Section 2.1.2, the eight "raw" stator signals, V_{xi}, can be combined to

form two signals which uniquely determine the rotor's in-plane position within one spatial period. These signals are

$$E_i = (V_{A1} + V_{C2}) - (V_{A2} + V_{C1}) \qquad (4-7)$$

$$E_q = (V_{B2} + V_{D1}) - (V_{B1} + V_{D2}) \qquad (4-8)$$

To get basic in-plane position signals, the rotor was moved in-plane in known increments using a micrometer. As it was moved, the amplitudes of the dither signals (V_{xi}) were measured. This was done over a range of 1 mm, which was close to 0.04", the spatial period. The V_{xi} signals from one of these measurements and resulting in-plane signals are shown in Figures 4.16-4.18.
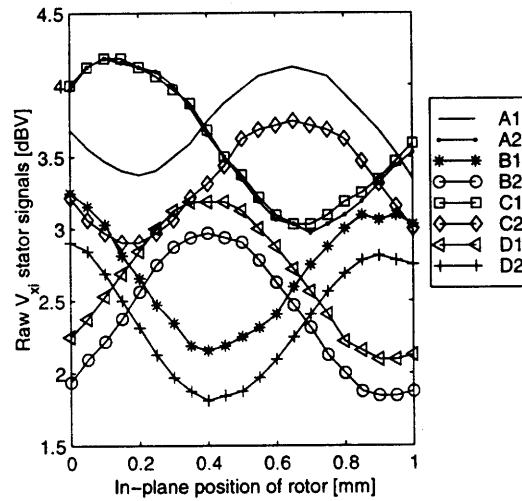
Figure 4.16: V_{xi} signals from oscilloscopes
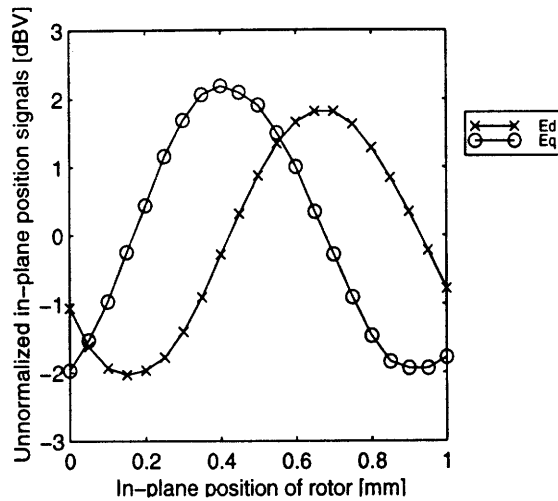
Figure 4.17: In-plane position signals (oscilloscope measurement)

As can be seen from Figure 4.16, the raw signals had various offsets, but roughly similar amplitudes. Because of the structure of Equations 4-7 and 4-8, the important thing was the differences between V_{x1} and V_{x2}, not their absolute magnitudes. Figure 4.18 shows the signals of Figure 4.17 normalized by a factor of $E_{norm} = \sqrt{E_d^2 + E_q^2}$, which is also plotted.
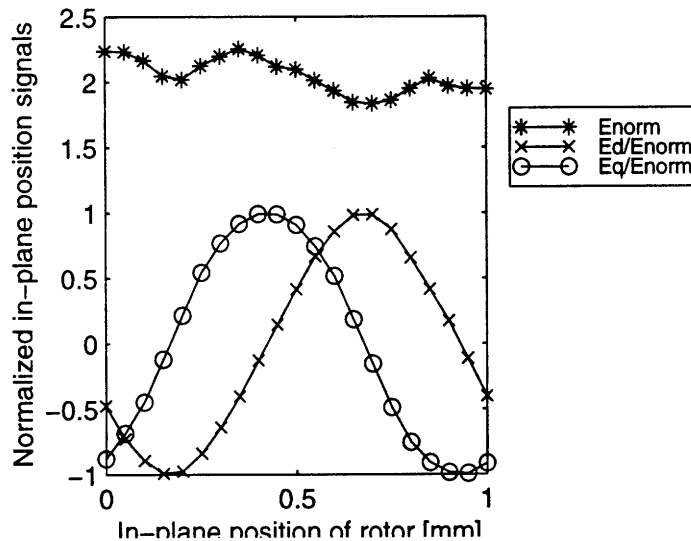
Figure 4.18: Normalized in-plane position signals (oscilloscope measurement)

The general shape of these curves was similar to those measured by Taussig in previous experiments, and agree with what one would expect. An interesting thing is that the normalizing factor gets smaller as the displacement gets closer to 1 mm. This happened regularly for many

measurements, because the gap changed slightly as the rotor was moved in-plane. This out-of-plane motion was unintentional and occurred because of twisting in the leaf springs suspending the rotor, and is explained more in the discussion on obtaining the gap signal. The next figure shows the fourier transform for the normalized E_d and E_q signals above. We can see that the signals are close to being pure sine waves, but are not perfectly pure. Given the near perfection, the inverse tangent function might be a good means of determining rotor position from the two signals. .
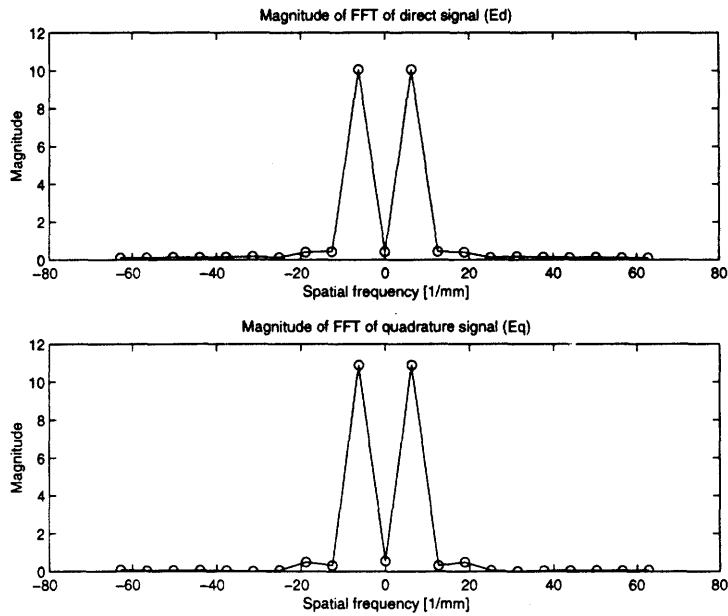
Figure 19: Fourier transforms of normalized E_d and E_q

The in-plane position-signal measurement was taken at a few different rotor gaps as follows:

1. The rotor-stator gap was set

2. In-plane positions were measured from 0 - 1 mm

3. The gap was changed.

4. In-plane measurements were repeated.

The results of these experiments show that the normalized E_d and E_q signals are indeed independent of gap. In Figure 4.20, we see that the in-plane position signals look the same

although they have been taken for three gaps.
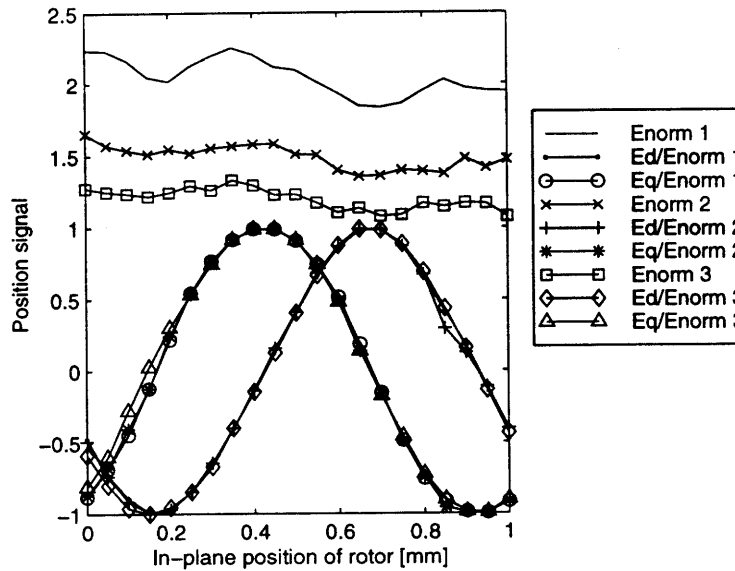
Figure 4.20: The in-plane position signals are independent of gap (oscilloscope measurement)

The gaps, numbered 1-3 from smallest to largest, were set to be roughly 0.010", 0.012", and 0.014". However, because of a flaw in the experiment the actual gaps were probably only 0.010", 0.011", and 0.012" respectively. This flaw was that the in-plane micrometer was allowed to touch the rotor, even when the gap was being changed (unlike the experiments of Section 3.4). Because of the added friction between the in-plane micrometer and rotor, the gap changed only about half the amount it should have changed according to the micrometer settings.

Gap signal using oscilloscopes

The out-of-plane rotor position signal, also known as the gap signal, was calculated by the method given in Section 2.1.2, described in the following equation:

$$E_{gap} = V_{A1} + V_{A2} + V_{B1} + V_{B2} + V_{C1} + V_{C2} + V_{D1} + V_{D2} \qquad (4-9)$$

Assuming that the gap was constant over varying in-plane positions, measurements of the gap for various in-plane positions were made. These measurements are shown below in Figure
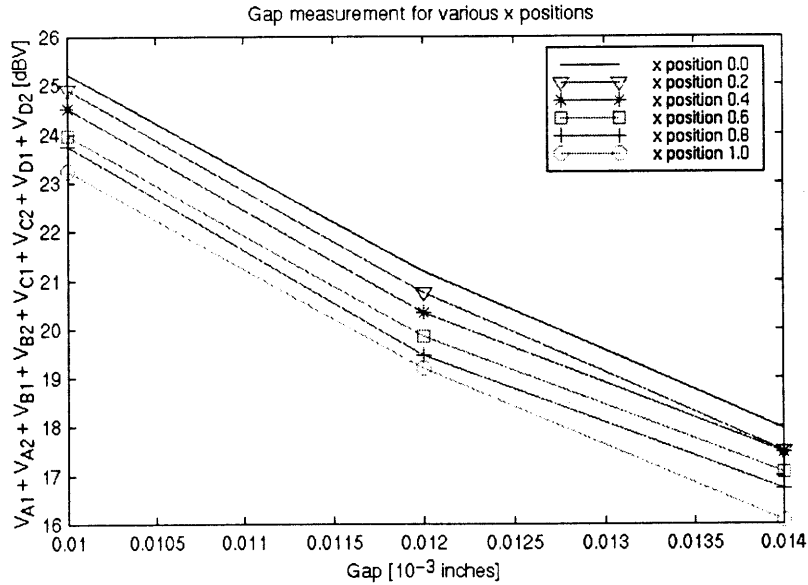
Figure 4.21: Gap signal using oscilloscopes

Again, the same flaw in the experiment occurred for the data in Figure 4.21 as for the data in Figure 4.20. Although the gaps were set to be 0.010", 0.012", and 0.014" (and are shown that way on the horizontal axis), in actuality they were probably only about 0.010", 0.011", and 0.012" respectively. Despite this problem, the graph clearly shows that the gap measurement is dependent on the in-plane position. In theory, this should not occur.

To see whether or not the gap really was dependent on the in-plane position, an independent method was used to measure the gap. The same beam-interrupt device used in Section 3.4 was again used to measure the rotor's out-of-plane position. In this experiment, the rotor was moved in-plane (with a constant gap setting). Two methods were employed to measure the gap: the beam-interrupt method (see Section 3.4) and the capacitive method based on

Equation 4-9. Figure 4.22 shows the results:

Capacitive and beam-interrupt position signals
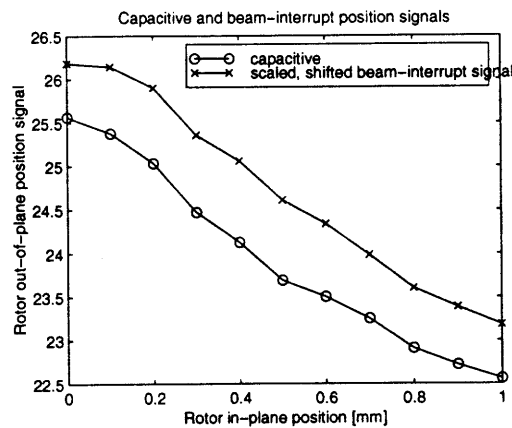
Figure 4.22: Gap's dependence on in-plane position

In Figure 4.22, both signals show a dependence of the gap on the in-plane position. Also, both signals have similar fine structure, which implies that the capacitive gap measurement is sensitive to small changes in gap and is reasonably accurate. This experiment confirmed that the gap really was changing with the in-plane position. The dependence probably occurred because the leaf springs were twisting as the rotor was moved by the in-plane micrometer.

Finally, an experiment was done to discover the stator voltages' dependence on gap. Half of the rotor electrodes were set to a periodic signal at 70 kHz, while the remaining rotor electrodes were grounded. Then, the peak-to-peak amplitude of the voltage on one stator phase (which was also at 70 kHz) was measured for various gaps. The results are shown below in Figure 4.23

Raw stator output vs. gap
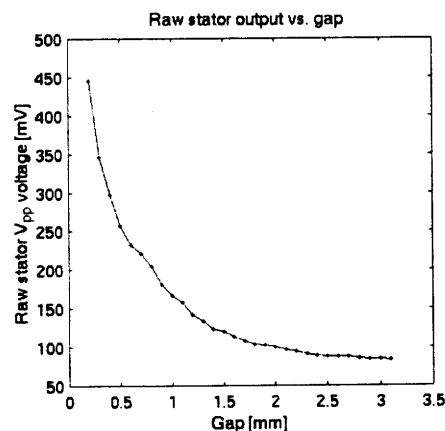
Figure 4.23: Direct stator signal amplitude as a function of gap

The shape of the curve is roughly a 1/x function, which is reasonable since the rotor-stator

capacitance is inversely proportional to the gap.

4.7.2 Position signals using the demodulator circuit

The next step was to connect the demodulator circuit directly to the stator phases, without using the RC crossover network as a go-between. Initially there was much difficulty in obtaining a good capacitive position signal. This was probably due to poor alignment of the rotor and stator. After changing the springs (from a thickness of 0.002" to 0.004"), changing the adhesive holding the rotor and stator to their mounts (from glue to tape), and realigning the rotor to the stator (so the gap was roughly 0.01"~0.015"), better signals were obtained. In addition to mechanical changes, minor electrical changes were made--the variable resistors for the bandpass filters were replaced with fixed resistors, making the gains of each channel slightly different. The resulting position signals are shown in Figure 4.24.
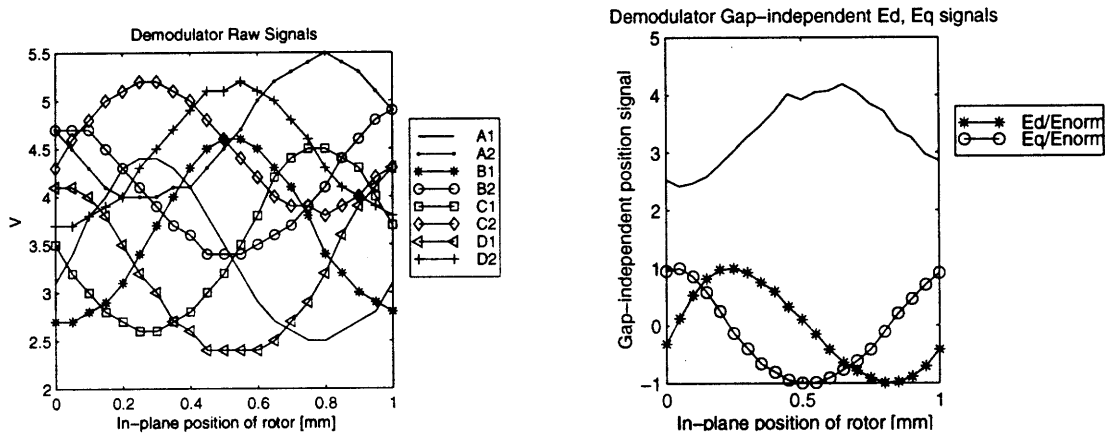
Figure 4.24: In-plane signals using demodulator circuit

The "raw" demodulator output signals shown in Figure 4.24 were the average values of the voltages on each demodulation channel as the rotor was moved in-plane. What is not shown in the figure is the noise on the output of each of these channels. This noise was roughly 0.2 V in amplitude. When compared with the roughly 1.5 V peak-to-peak amplitude of the "raw" demodulator output signals, this noise seemed acceptable. Minimizing the noise was important, because the signal would be sampled by the DSP and converted to a digital signal.

Although the signals of Figure 4.24 looked reasonable, they were somewhat distorted compared to the signals obtained when the oscilloscopes were used instead of the demodulator circuit. The reason for this was not clear, although it could have been because of saturation in some of the channels or slightly mismatched frequencies. Figure 4.25 shows the fourier

transform of the normalized E_d and E_q signals.

Magnitude of FFT of direct signal

Magnitude of FFT of quadrature signal
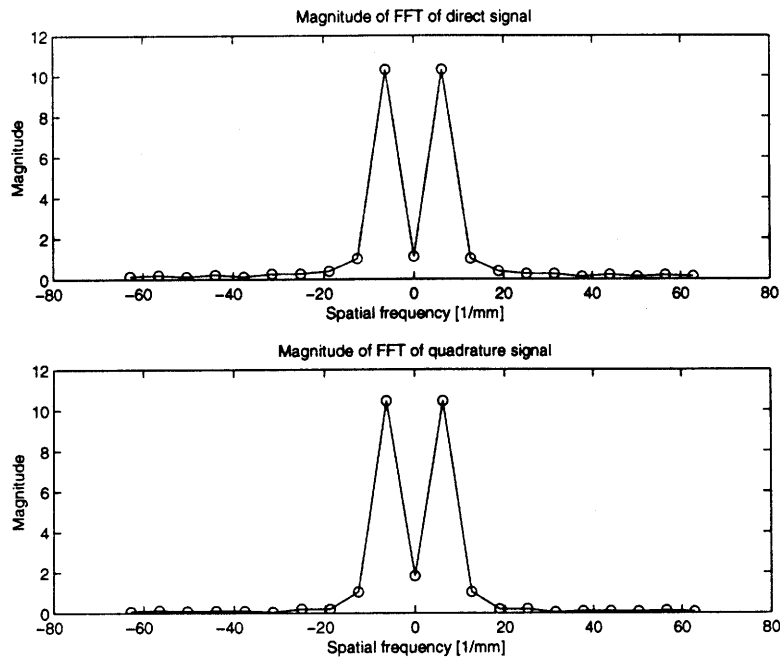
4.25: Fourier transform of normalized E_d, E_q signals
measured using the demodulator.

One concern was that different gains on the eight different demodulation channels would cause a distorted signal. However, differing channel gains do not actually cause distortion of the E_d/E_{norm} and E_q/E_{norm} signal shapes. Instead, the method used to calculate E_d/E_{norm} and E_q/E_{norm} actually helps average and divide out the gains of the channels, as seen from Equations 2-9, 2-10, and 2-11.

4.7.3 Estimating the accuracy of the position measurement

So far, E_d/E_{norm} and E_q/E_{norm} have been used to describe the in-plane rotor displacement. However, these two signals must still be translated into an actual displacement. There are a few ways this could be done. One way involves creating a lookup table and assigning a displacement to each E_d/E_{norm} and E_q/E_{norm} combination. Another method involves taking the inverse tangent

of arctan(E_q/E_d). When this is done using the data of Figure 4.24, the following figure results:
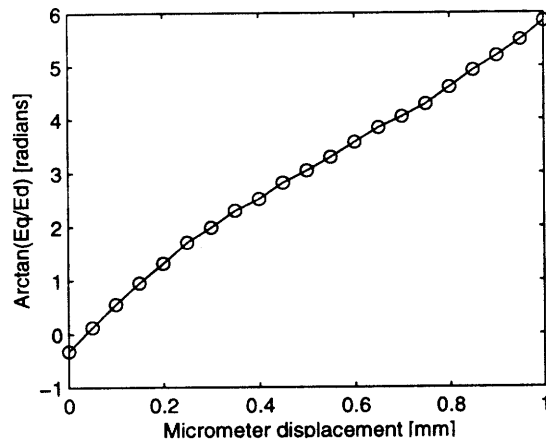
Figure 4.26: Arctan of E_q and E_d, without noise

Ideally, the plot in Figure 4.26 should be a perfectly straight line. However, most likely because of measurement system error, the line is curved. When a least-squares-fit straight line is subtracted from the curve in Figure 4.26, the least-squares error remains and is shown in Figure 4.27.
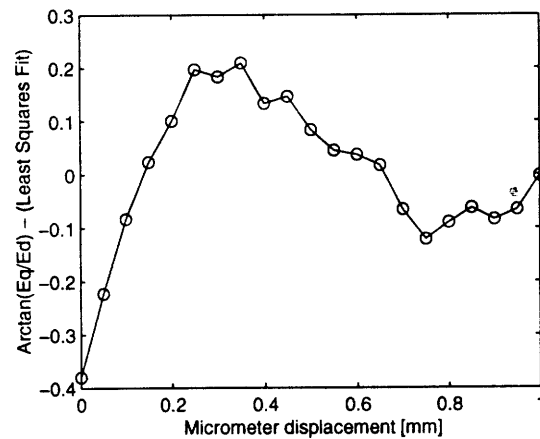
Figure 4.27: Least-squares error of position measurement

From Figure 4.27, the maximum error in the measurement is approximately 0.4 radians, which corresponds to about 0.06 mm or 6%.

In summary, the demodulator circuit was hooked directly to the motor, and an in-plane position signal was successfully read. Although out-of-plane signals were not measured, it is likely that the gap signal could also be measured in this setup, since the basic in-plane signal was

successful, and the out-of-plane signal is calculated from the same V_{xi} components. The next step would be to hook the demodulator circuit to the RC crossover network, which would be needed during actual motor operation to protect the demodulator from the motor's high voltages. This step has not yet been performed due to time constraints. The RC crossover network is discussed in Chapter 6.

5.0 Driving the motor: High-voltage circuitry

5.1 Purpose of high-voltage circuitry

This chapter describes the motor's high-voltage drive circuitry, shaded gray in the following diagram.
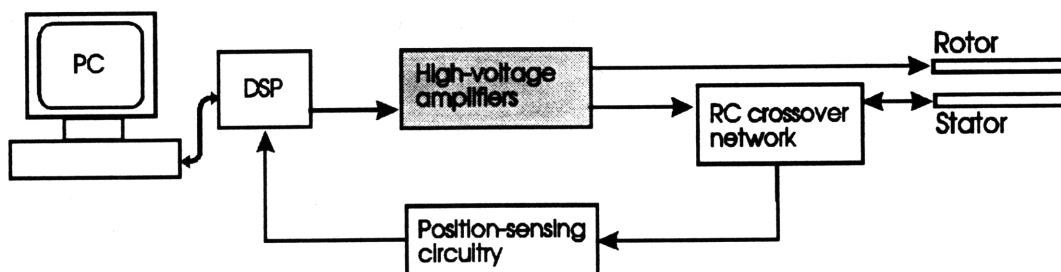
Figure 5.1: System block diagram; high-voltage circuitry is shaded

The purpose of these amplifiers was to generate the motor's drive voltages (~400 V) from low-voltage (0 - 10 V) input signals. For the stator, the low-voltage signals would come from the DSP, as shown in Figure 5.1 For the rotor, the low-voltage signals would be a constant DC voltage plus a high-frequency dither (carrier) signal.

5.2 Design

The following diagram shows the basic design of the high-voltage amplifier.
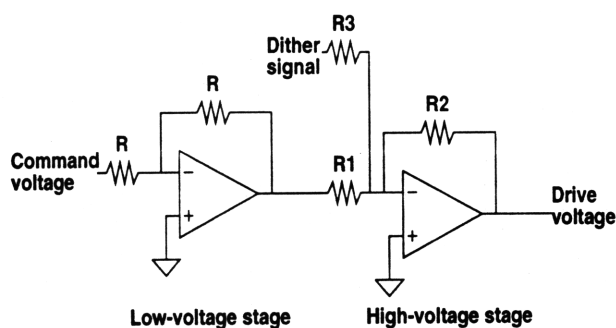
Figure 5.2 High-voltage inverting amplifier

The figure shows the amplifier for the rotor. The amplifier for the stator is the same, but with R_3=infinity --there is no dither signal on the stator. The amplifier consists of two stages: 1) a unit-

gain low-voltage inverting amplifier and 2) a high gain, high-voltage inverting amplifier. The inverting design for the high-voltage amplifier was chosen because it provided better performance during experimental tests. Six separate amplifiers were needed: one for each of the four stator phases, and one for each of the two separate rotor traces. Each of the amplifiers for the stator had a single input which was to come from the DSP. Each of the amplifiers for the rotor had two inputs (dither frequency signal for position-sensing, as well as a constant DC voltage for the drive) and summed them.

5.3 Experimental details

5.3.1 Parts and construction

A more detailed schematic diagram than Figure 5.2 is shown in Appendix C.

First stage: inversion of input signal

AD711 low-voltage op-amps were used to invert the incoming signal.

Second stage: high-voltage amplification

Apex PA85 power op-amps were used to perform the high-voltage amplification. They were MOSFET op-amps used with a single-sided power supply (0 to 400 V). Because they were high-power devices, the amplifiers had to be mounted on large heatsinks, which were mounted to a large aluminum plate. The PA85 op-amps required a few external resistors and capacitors for phase compensation. In addition, bypass capacitors were used on the power-supply pins. High-voltage resistors and capacitors were used for these external components, which were soldered to the pins of each PA85 op-amp.

The components used in the PA85 op-amp stage are listed in Tables 2 and 3.:

Table 2: External components directly soldered to PA85

Component Name	Value	Purpose
R_C	196 kΩ	phase compensation
C_C	3.3 pF	phase compensation
R_L	28.7 Ω	current-limiting resistor
C_B	100,000 pF	bypass capacitor

Table 2: External components directly soldered to PA85

Component Name	Value	Purpose
C_B	100,000 pF	bypass capacitor

Table 3: Components used for high-voltage inverting setup

Component Name	Resistance [kΩ]	Signal being amplified
R_1	2.51	Stator
R_2	100	Stator
R_3	infinity (no dither)	Stator
R_1	2.51	Rotor
R_2	100	Rotor
R_3	26.8	Rotor

The high-voltage inverting stage was designed to have a gain ~ 40. From this, the phase compensation capacitor and resistor (C_C and R_C) were chosen roughly according to guides in the part specifications. The slew rate, which relies on C_C, was expected to be roughly 700 V/μs, much faster than needed for this application. R_L, the current-limiting resistor, was chosen so that the current would be limited as much as possible (0.04 A).

The additional wiring and components needed to form the inverting configuration were initially built onto a single board, but the amplifiers were unreliable in this setup. The circuit was not stable and was sensitive to wires being touched or moved. Later, the wiring for each amplifier was done on separate boards, one for each amplifier. Each small board was mounted very close to its corresponding PA85 op-amp. This made the circuit more robust and less prone to change if the setup was jostled. Stability was improved since the bypass capacitors were plugged into the boards, and these capacitors had to be physically close to the op-amps in order to be helpful.

5.3.2 Testing

Some preliminary tests were done, only at low voltages. All six amplifiers were tested. Test inputs were connected directly to the PA85 amplifier stages. The amplifiers intended for the stator were fed 1 kHz signals, while the amplifiers for rotor were fed signals at 70 kHz and 95 kHz. The gain at DC was not measured for either the stator or the rotor. The gain for the stator amplifiers was around 33 instead of the expected 38. The gain for the rotor amplifiers was around 5 instead of the expected 4. So, the amplifiers roughly worked as expected, but further testing should be done at DC input voltages and at higher voltages.

During testing, it was also found that the PA85 op-amp performance was dependent on the bypass capacitor values. When alternate bypass capacitors were substituted, oscillations occurred even though R_c and C_c were used for phase compensation.

6.0 RC crossover network

In this chapter, the RC crossover network (shaded below) is discussed.
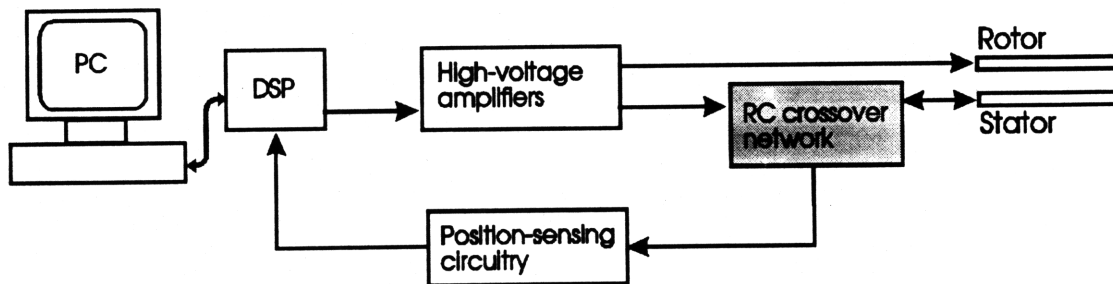
Figure 6.1: System block diagram; RC network is shaded

The chapter first describes the circuit's purpose and design criteria. It continues by describing the basic circuit, modeling, and some experimental testing. Finally, improvements and revisions to the circuit are suggested.

6.1 Purpose

Each block in Figure 6.1 works within a certain voltage range. The high-voltage amplifiers put out voltages around 400 V, while the position-sensing circuitry operates at low voltages, less than 20 V. Both of these blocks must be connected to the stator electrodes. However, there are two reasons why the high-voltage and position-sensing circuitry should not be connected directly to the stator electrodes. First, if the high-voltage amplifiers were directly connected, the stator electrodes would not be free to pick up the high-frequency carrier waves on the rotor that are necessary for this position-sensing scheme. In short, the position-sensing scheme would not work. Second, if the high-voltage and position-sensing circuitry were both directly connected to the electrodes, it is possible that a high current could flow from the high-voltage section to the position-sensing circuitry, damaging the latter.

In order to avoid these problems, a go-between circuit must be placed between the high-voltage amplifiers, the position-sensing circuitry, and the stator itself. The RC crossover network is only one possible implementation of this circuit. Other designs, perhaps involving active elements, may perform better. The RC network design was explored here partly because of its simplicity -- it only contains passive resistors and capacitors. In addition, this simplicity may add

robustness, because there are fewer parts that can fail.

6.2 Design and testing

6.2.1 Design criteria

Ideally, the RC crossover network would perfectly meet the following criteria:

1) Allow the low-frequency, high-voltage drive signal to reach the stator electrodes unattenuated.

2) Allow the high-frequency, low-voltage position signals detected by the stator to reach the position-sensing circuitry unattenuated.

3) Prevent the high-voltage stator drive voltages from reaching the position-sensing circuitry, to prevent damage.

In addition, each of these three descriptive criteria have corresponding quantitative requirements. The low frequencies correspond to the drive signals, and are less than 1 kHz. The high frequencies correspond to the dither signals and are around 70-100 kHz. In reality there is likely to be some unwanted attenuation in Criteria 1 and 2, and some transmission of the drive signals to the position-sensing circuitry. In Criterion 1, the amount of attenuation will limit the maximum motor forces. In Criterion 2, the amount of allowable attenuation is dictated by two things: 1) the maximum allowable amplitude for the position signals and 2) the minimum signal detectable by the position-sensing circuitry. Finally, in Criterion 3, the position-sensing circuitry should be fine if the drive signals are reduced to the voltage range of the position signal, and if the drive signal does not have a high current.

6.2.2 Initial design

The following circuit is based on a design by Taussig, except the capacitance C_b has been added. In the diagram, R_b and C_b are not actual circuit elements, but models of the next stage in the signal path. However, R and C do represent actual, discrete components used in the circuit

that was built.
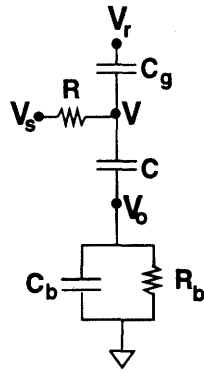
Figure 6.2: Initial RC circuit

where V_r = voltage on rotor

V_s = drive voltage "command" to stator (from high-voltage amplifiers)

V = actual voltage on stator

V_o = voltage going to position-sensing circuitry

C_g = gap capacitance between one stator phase and one rotor phase

C_b = model of input capacitance of next stage (position-sensing circuitry)

R_b = model of input resistance of next stage (position-sensing circuitry)

C = capacitor in RC network

R = resistor in RC network

An initial glance at the circuit in Figure 6.2 tells how the circuit works. The low-frequency signals of V_s get transmitted to V (the stator), but less to V_o (position-sensing circuitry). The high-frequency signals on V_r get transmitted to V_o. Of the resistors and capacitors listed above, we have some control over R_b and C_b, but the main design parameters are R and C. C_g is the gap capacitance of the motor, which varies for different rotor positions.

6.2.3 Choosing component values: intuitive approach

In terms of the criteria of Section 6.2.1:

1) V/V_s must be a lowpass filter (needed for good actuation);

2) V_o/V_r must be a highpass filter (needed for good sensing);

3) V_o/V_s must have attenuation at low frequencies (needed to protect sensing equipment).

For each filter, the cutoff frequency should be above the drive frequency (f_m), yet smaller than the dither frequency (f_1, f_2). How do these criteria affect our choice of R and C, assuming that R_b, C_b, and C_g are given? It is possible to calculate complete transfer functions (see Section 6.2.4). However, because these expressions are large, it is difficult to gain intuition from them. Instead, we will first look at simplified approximate transfer functions.

Examining V/V_s

The high-voltage, low-frequency drive signal on V_s must be transmitted to V with little attenuation to support good actuation. Assuming that $1/j\omega C_g$ is large, the circuit can be viewed as follows:

$$Z_1 = R$$

$$Z_2 = \frac{1}{j\omega C} + \frac{R_b}{1 + j\omega R_b C_b}$$
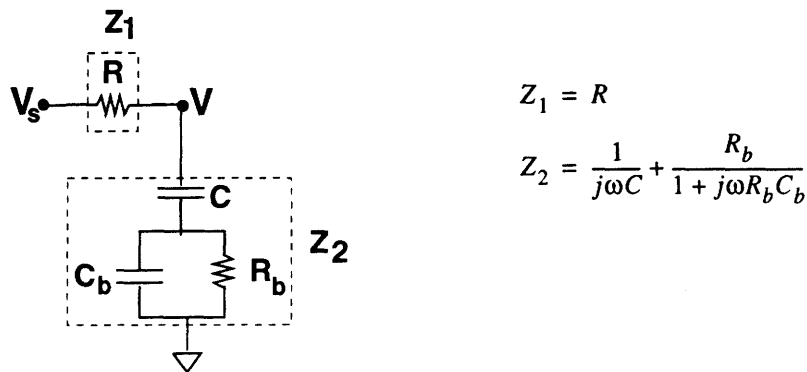
Figure 6.3: Simplified circuit for transfer function V/V_s

Since $|V/V_s| = |Z_2/(Z_1+Z_2)|$, we want $|Z_2| > |Z_1|$ at low frequencies. Assuming that R_b and C_b are fixed, $1/\omega C$ should therefore be small compared with R.

Examining V_o/V_r

$|V_o/V_r|$ should be as high as possible at high frequencies (dither frequencies f_1, f_2) to support good position-sensing. Assuming that R is large, the following approximate circuit can

be drawn:

$$Z_1 = \frac{1}{j\omega C} + \frac{1}{j\omega C_g}$$

$$Z_2 = \frac{R_b}{1 + j\omega R_b C_b}$$
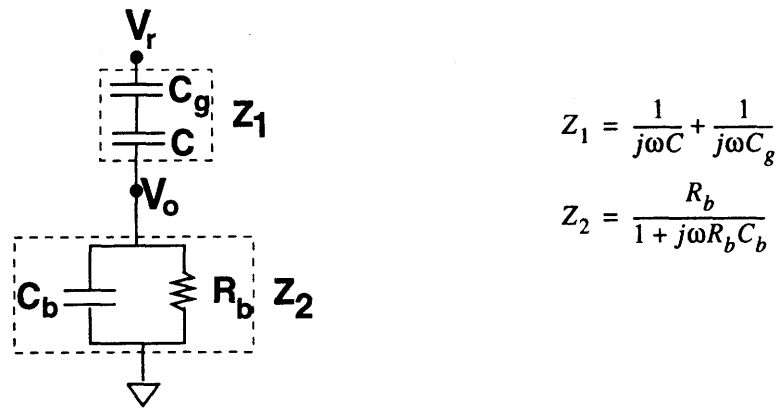
Figure 6.4: Simplified circuit for transfer function V_o/V_r

We want $|Z_2| > |Z_1|$ at high frequencies to maximize $|V_o/V_r|=|Z_2/(Z_1+Z_2)|$ at high frequencies. Assuming that R_b, C_b, and C_g are fixed, a large ωC should be chosen to minimize Z_1. However, because C and C_g are in series, Z_1 will ultimately have the impedance of C_g, no matter how large C is.

Examining V_o/V_s

Finally, the high-voltage, low-frequency voltage V_s should not be transmitted to V_o, in order to protect the position-sensing circuitry. Again assuming the impedance of C_g is large at low frequencies, the circuit can be viewed as follows:

$$Z_1 = R + \frac{1}{j\omega C}$$

$$Z_2 = \frac{R_b}{1 + j\omega R_b C_b}$$
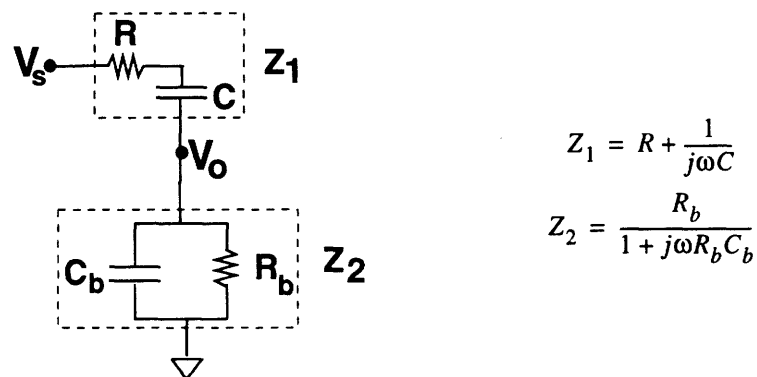
Figure 6.5: Simplified circuit for transfer function V_o/V_s

In this case, $|V_o/V_s|$ should be small for low frequencies. To achieve this, $|Z_1| > |Z_2|$. R should be

large, and ωC small.

Summary

In summary, at low frequencies, it is desirable to have R large and ωC small. At high frequencies, ωC should be large. Fortunately, it happens that these requirements are simultaneously achievable.

6.2.4 Complete transfer functions

The transfer functions V/V_s, V_o/V_s, and V_o/V_r can be calculated as follows:

$$V = H_s(j\omega)V_s + H_r(j\omega)V_r \qquad (6-1)$$

where H_s, H_r are

$$H_s(j\omega) = \frac{R_b(C_b + C)j\omega + 1}{1 - R_b R[C_g C + C_b(C + C_g)]\omega^2 + [R_b(C + C_b) + R(C + C_g)]j\omega} \qquad (6-2)$$

$$H_r(j\omega) = \frac{-R_b R C_g(C + C_b)\omega^2 + R C_g j\omega}{1 - R_b R[C_g C + C_b(C + C_g)]\omega^2 + [R_b(C + C_b) + R(C + C_g)]j\omega} \qquad (6-3)$$

Also,

$$V_o = H(j\omega)V = H(j\omega)[H_s(j\omega)V_s + H_r(j\omega)V_r] \qquad (6-4)$$

where

$$H(j\omega) = \frac{R_b C j\omega}{1 + R_b(C + C_b)j\omega} \qquad (6-5)$$

Therefore, the three transfer functions of interest are

$$\frac{V}{V_s} = H_s(j\omega) \qquad (6-6)$$

$$\frac{V_o}{V_s} = H(j\omega)H_s(j\omega) \qquad (6-7)$$

$$\frac{V_o}{V_r} = H(j\omega)H_r(j\omega) \qquad (6-8)$$

Finally, the magnitudes of these transfer functions are shown below.

$$\left|\frac{V}{V_s}\right| = \sqrt{\frac{[R_b(C_b+C)\omega]^2+1}{\left\{1-R_bR[C_gC+C_b(C+C_g)]\omega^2\right\}^2+\{[R_b(C+C_b)+R(C+C_g)]\omega\}^2}} \qquad (6-9)$$

$$\left|\frac{V_o}{V_s}\right| = \sqrt{\frac{[R_b(C_b+C)\omega]^2+1}{\left\{1-R_bR[C_gC+C_b(C+C_g)]\omega^2\right\}^2+\{[R_b(C+C_b)+R(C+C_g)]\omega\}^2}}\sqrt{\frac{(R_bC\omega)^2}{1+[(R_b(C+C_b)\omega)]^2}}$$

$$(6-10)$$

$$\left|\frac{V_o}{V_r}\right| = \sqrt{\frac{[R_bRC_g(C+C_b)\omega^2]^2+(RC_g\omega)^2}{\left\{1-R_bR[C_gC+C_b(C+C_g)]\omega^2\right\}^2+\{[R_b(C+C_b)+R(C+C_g)]\omega\}^2}}\sqrt{\frac{(R_bC\omega)^2}{1+[(R_b(C+C_b)\omega)]^2}}$$

$$(6-11)$$

The above expressions are unwieldy, and it is difficult to obtain any design intuition from them as was gained in the previous section. However, these formulas are useful for simulating the transfer functions and seeing how well the model fits with the experiment, discussed next.

6.2.5 Comparison between model and experiment

To see how closely the equations of 6.2.4 describe reality, the circuit of Figure 6.2 was built with components shown in Figure 6.3. Using this circuit, the magnitudes of the transfer functions $H(j\omega)$, $H_s(j\omega)$, and $H_r(j\omega)$ were measured and compared against the expected values. The general shapes of H_r (highpass), H_s (lowpass), and H (highpass) can be predicted intuitively

from the design criteria.
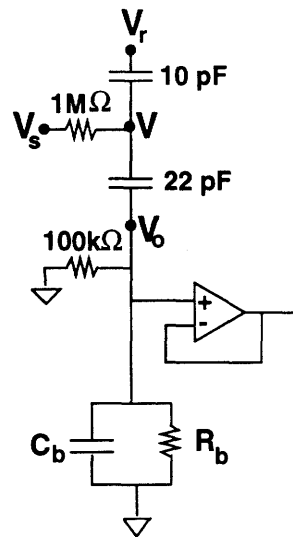
Figure 6.6: Experimental RC circuit

Figure 6.6 shows the circuit that was built. The components with actual values represent physical parts that were used. R_b, C_b, and the ideal buffer represent an op-amp follower which was the next stage in the signal path. The next few sections explain how the components for the experiments were chosen, and how R_b and C_b were estimated or measured.

Estimating values of "fixed" components R_b, C_b, C_g

Initially, the 100kΩ resistor shown in the diagram was not included, and R_b was the input resistance of the op-amp follower. However, in this configuration, R_b was estimated to be huge ($\gg 10^{12}$Ω) from op-amp data sheets. This was bad, because we can see from Figure 6.2 that R_b, C_b, and C create a voltage division between V_o and V. Examine Equation 6-5. Suppose $R_b(C+C_b) \gg 1$. In that case, $H(j\omega) \sim C/(C+C_b)$. This is undesirable, because $H(j\omega)$ must be a high-pass function, to protect the position-sensing circuitry from the high drive voltages. To correct this, a lower value of R_b was chosen by inserting the 100 kΩ resistor shown in Figure 6.6

C_g was estimated to be around 10 pF from the dimensions of the motor as described in Section 3.1.

C_b was estimated to be roughly 20 pF from preliminary measurements, described below.

Measuring C_b

C_b was measured by hooking the op-amp to a simplified circuit containing only a known C, shown below in Figure 6.7. The input/output transfer function is

$$\frac{V_o}{V_i} = \frac{R_b C j\omega}{1 + R_b(C + C_b)j\omega} \qquad (6-12)$$

The transfer function was measured. For high frequencies, V_o/V_i approaches a constant: $C/(C+C_b)$. This constant was measured, and C_b was extracted.
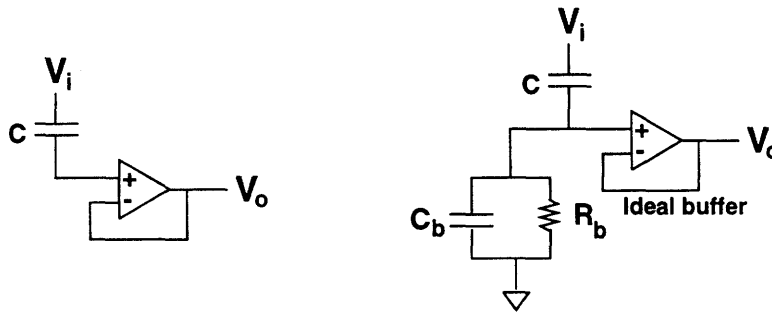
Figure 6.7: Simplified circuit for measuring C_b.
Actual circuit (left); circuit with C_b, R_b explicitly shown (right)

Experimental Results

After measuring C_b, values for R and C were chosen to create the desired filters, but they may not have been the optimum values. The component values were chosen as shown in Figure 6.6. A 10 pF capacitor was used for C_g instead of the actual rotor/stator capacitance, because the motor was not set up at the time the test was done.

Then $H(j\omega)$, $H_s(j\omega)$, and $H_r(j\omega)$ were calculated and compared against experimentally measured data. The following three graphs compare the analytical calculations with

experimental results.
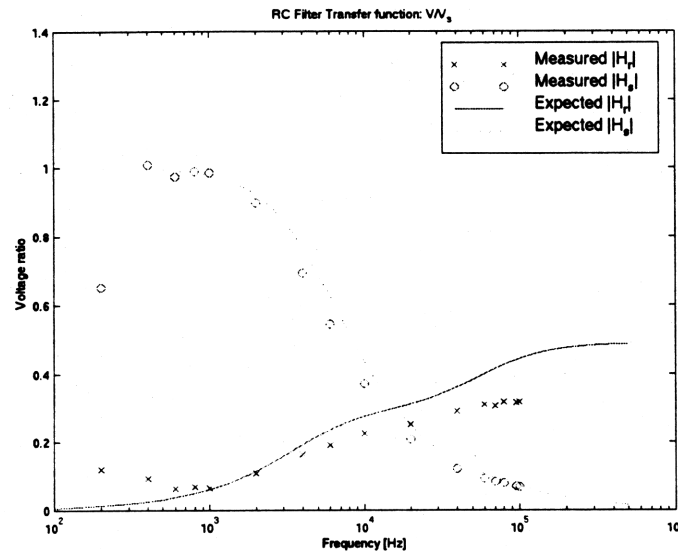
Figure 6.8: Measured vs. expected $|H_r|$, $|H_s|$

Figure 6.8 shows the measured and expected transfer functions between the stator node (V) and the rotor input (V_r) and stator input (V_s). The experimental points for this graph was not directly measured, but was calculated from direct measurements in Figures 6.9 and 6.10. We can see that the experimental curves are similar but not the same as the expected curves. In particular, the experimental value of $|H_s|$ deviates sharply from the expectation at the lowest measured frequency (located at f~200 Hz, Voltage ratio~0.65). Although this point on the graph may look like an error, it was repeatedly found on graphs of similar data sets. Since the experimental points of Figure 6.8 were not measured directly, it is possible that this outlying point is due to error. To investigate further, direct measurements of $|H_r|$ and $|H_s|$ should be taken. If the outlying point remains, this implies there is some behavior at low frequencies which the model does not account for, a serious problem which needs to be addressed However, for drive frequencies between 400-1000 Hz, the performance is quite good with a gain of nearly 1. The overall rotor transfer function seems to have roughly the right shape, but the gain is lower than expected, and the

measured values are higher than expected at low frequencies.
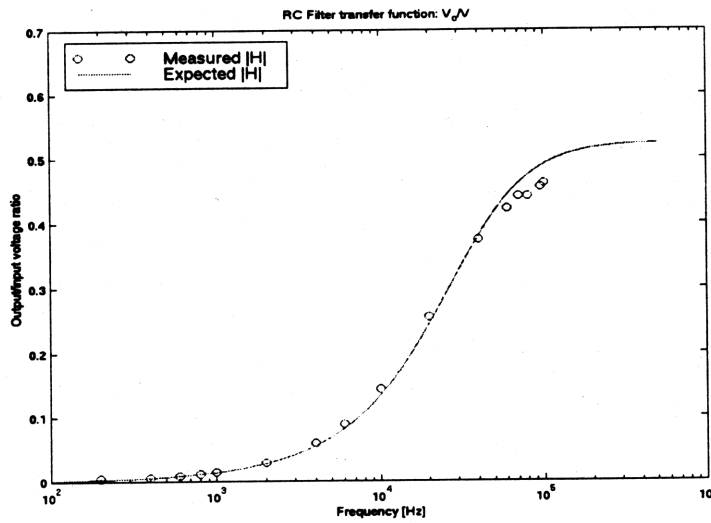
Figure 6.9: Measured vs. expected |H|

The measured values fall mostly on the expected curve in Figure 6.9. The next figure shows the transfer functions between the output and the stator drive and rotor dither inputs..
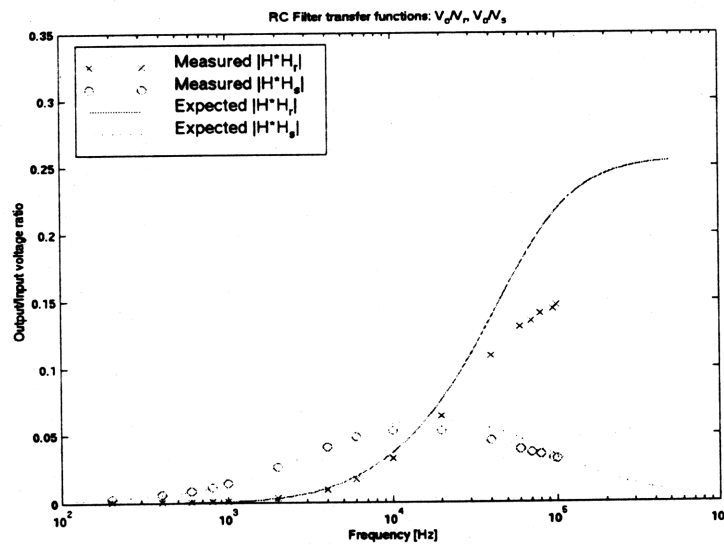
Figure 6.10: Measured vs. expected $|V_o/V_s|$, $|V_o/V_r|$.

Are the results in Figure 6.10 acceptable or poor?

First consider $|V_o/V_s|$. $|V_o/V_s| < 0.014$ for $\omega < 1$ kHz (from data in Figure 6.7). If $|V_s| = 400$ V, then $|V_o| < 5.6$ V, an acceptable voltage to put on the input of the position-sensing circuitry.

Next consider $|V_o/V_r|$. If the dither signals used are at 70 kHz and 100 kHz, $|V_o/V_r|=$ 0.1346 at 70 kHz and $|V_o/V_r|=0.1465$ at 100 kHz. Consider the worst case at 70 kHz, where the attenuation is greater. In order to judge whether these gains are acceptable or not, two quantities must be estimated: the largest allowable dither voltage amplitude and the smallest detectable position-signal amplitude. From Section 2.1.2, the motor forces scale as the square of the maximum drive voltage. Therefore, if the maximum drive voltage is 400 V, a 20 V dither signal will only alter the forces by 0.25%. A 40 V dither signal will only alter the forces by 1%. Say a dither signal of amplitude 20 V is chosen. In this case, a dither signal of amplitude 2.69 V would be input to the demodulator. We know from Section 4.7.2 that the demodulator has a noise amplitude at the output of 0.2 V, so it should be able to detect input signals 2.69 V in amplitude. From this analysis, the RC crossover network does perform adequately for this system in terms of position-sensing. However, in terms of driving the stator, the circuit only performs well for drive frequencies above 200 kHz according to the data in Figure 6.8.

Finally, it should be noted that the circuit design and components in this example have not been formally optimized, so it possible that better performance could be achieved. Other circuit designs were not explored because of time constraints. Sections 6.2.7 and 6.2.8 discuss minor revisions to the circuit and model.

6.2.6 Dependence on C_g

So far we have considered C_g to be a constant, roughly equal to 10 pF. However, the goal of the position-sensing method is to detect changes in C_g. How do the RC crossover network functions depend on C_g? The next graph shows the gain, $|V_o/V_r|$, evaluated at two frequencies ($f_1=70$ kHz and $f_2=95$ kHz) and $|V_o/V_s|$ evaluated at the frequency $f_m=1$ kHz. The values shown in the graph are calculations, not measurements. These calculations were made using the same

component values used in the previous section.

RC pass characteristics for variable C_g at key frequencies
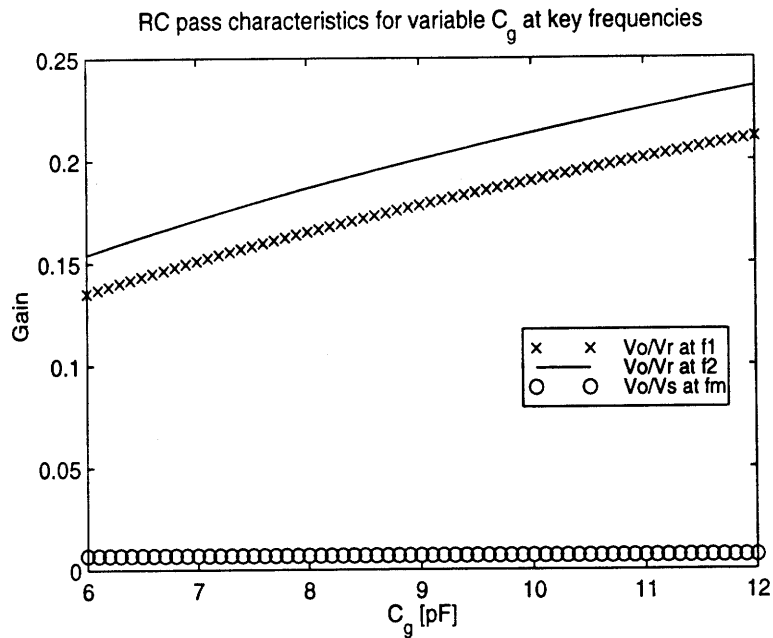
Figure 6.11: Expected dependence of crossover network characteristics on C_g

We can see that, for a given capacitance, the gain $|V_o/V_r|$ evaluated at f_2 will always be higher than that evaluated at f_1. (This could also be seen from Figures 6.8-10.) Figure 6.11 also tells us how much $|V_o/V_r|$ changes as C_g changes. In order for either in-plane or out-of-plane position-sensing to occur, the $|V_o/V_r|$ curves of Figure 6.11 must have a non-zero slope, and preferably a large slope. Without a non-zero slope, the system will not be able to distinguish between different gap capacitances, and position-sensing will fail. This is because all the position information is embodied in C_g, which depends on both the in-plane and out-of-plane separation between the rotor and stator.

6.2.7 Revising the model: accounting for a ground plane

Once the motor was assembled, it was realized that there was a capacitance between the stator electrodes and the stator ground plane which was not accounted for in the model. (The similar rotor ground-plane capacitance doesn't affect this circuit model.) To account for this

ground-plane capacitance C_{gp}, the model was modified as shown below.
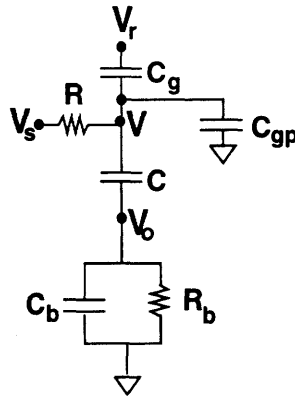
Figure 6.12: Revised RC circuit with ground-plane capacitance

The transfer functions of Equations 6-2 and 6-3 were also modified. In the denominators of each transfer function, C_g was replaced with C_g+C_{gp}. The effect of including C_{gp} is that the overall transfer function V/V_r is smaller in magnitude (because of the role of C_{gp} in the voltage divider). In other words, the performance of the circuit worsens slightly, but the overall shape of the filters remains the same.

6.2.8 Revising the circuit: protection against shorting and voltage spikes

Finally, some thought was given to the problem of shorting between electrodes (both on the rotor and stator) and of providing more protection for the position-sensing circuitry from high currents due to the high-voltage section. Note that there are a few different ways the electrodes could short (stator-stator, rotor-rotor, rotor-stator). This type of shorting is a definite danger with the current setup, because of the exposed metal electrodes and sensitive mechanical setup.

Possible solutions include 1) limiting the current coming out of the high-voltage power supply before it ever reaches the drive circuitry (this could be done with a resistor or something fancier) and 2) inserting a resistor in the RC circuit connected to the V_o node and in series with a inverting amplifier that leads to the position-sensing circuitry. Voltage-clamps involving diodes were also considered.

However, none of these options was explored in detail, and more work must be done. In addition, no position measurements were made with the RC crossover network inserted into the system. As mentioned at the beginning of Section 4.7, this next step did not occur because of

limited time. Performing this step would likely introduce more modifications to the circuit.

7.0 Summary, conclusions, and suggestions for future work

7.1 Summary

A design by Carl Taussig for a linear electrostatic micromotor with forces in both the in-plane and out-of-plane directions was described in Section 2.1. In addition, a method for detecting the motor's position by measuring capacitance was also explained in Section 2.1. In Chapter 3, the experimental setup for this thesis was described. A scaled-up prototype of the motor was built, and the electronics necessary for driving the motor and extracting a feedback signal were designed and built. These electronics fell into three parts: a demodulator for the position signal, drive amplifiers, and an RC crossover network to interface the other two parts to the motor and were described in Chapters 4, 5, and 6 respectively. The demodulator was used to successfully measure a position signal from the motor model in Section 4.7.2.

7.2 Conclusions

The main result of the thesis is the demonstration of the basic position-sensing scheme with an in-plane measurement accuracy of about 6%, or 0.06 mm using the demodulation circuitry connected directly to the stator electrodes. The demodulation circuitry was tested and behaved as expected, but could be optimized further.

The high-voltage drive amplifiers were stable and gains were as expected during low-voltage tests.

The RC crossover network provided adequate performance for the design requirements for drive frequencies greater than 400 Hz only. Specifically, the drive signal was transmitted from the stator drive input to the stator with an attenuation of 0.65 for a 200 Hz drive signal, according to measurements in Figure 6.8. This was not acceptable performance, and more measurements should be taken, including direct measurements of the transfer function between the stator electrode and the drive input to the stator. However, for drive signals between 400-1000 Hz, the gain was excellent (between 0.98 and 1.00). The drive signal was adequately attenuated by a factor of 0.014 or less, which was enough to protect the position-sensing circuitry from high voltages. Finally, the position signal from the rotor was attenuated by a factor of about 0.15 in the worst case, which still left a large enough signal for the position-sensing circuitry to detect. Overall, the RC crossover network worked well except for low drive frequencies around 200 Hz.

Overall, information was gained on how to improve the electronics for the scaled-up motor model. These findings may or may not be directly applicable to the electronics for an actual-size micromotor. In particular, the measurement of the capacitance may become a much trickier issue when dealing with tiny micromotor capacitances. However, the goal of the current project was not to build an electronics system exactly like the one to be used for the micromotor. Instead, the goal of the current project was to create electronics for a scaled-up model, so that further work can be done on investigating motor control issues.

7.3 Suggestions for future work

Looking at the big picture, this project is a step toward reaching the goal of a fully-working motor prototype. However, to reach that goal, these further steps must be completed:
- Improvement of electronics
- Integration of electronics with DSP control
- Development of control algorithms

Specific suggestions on improving the electronics have been interspersed throughout the text. In particular, the bandpass filter of the demodulator should be upgraded to a higher-order filter. The high-voltage drive circuitry should be tested at high voltages, and the 0 dB gain should be measured. If the current RC crossover circuit cannot achieve acceptable performance for low frequency drive signals, alternate circuit designs to the RC crossover network should be investigated. Finally, more consideration and experimentation should be given to the problem of high voltage shorting between electrodes and of how to protect the position-sensing circuitry from high currents. In general, all circuits should be experimented with further, and the designs should be improved if necessary.

One improvement to the motor design which was not mentioned in the text involves changing the layout of the electrodes on the rotor or stator. The rotor or stator plane could be divided into quadrants, with the electrodes on each quadrant electrically separate from those on the other quadrants. (Actually, the pattern might be a little more complicated, but this is the basic idea.) All electrodes would still look like long, skinny lines and would be connected in the four-phase periodic manner. This configuration would give greater precision in position-sensing, because it would also tell how parallel the rotor and stator planes are by providing four separate gap-distance signals. This electrode grouping would increase the number of position signals,

increasing the complexity of the design. However, it might be beneficial, because it would be easier to align the rotor to the stator and ensure the planes were parallel.

References

[1] L.S. Fan, Y,C. Tai, and R.S. Muller, "IC-processed electrostatic micro-motors", *Proc. of the 1988 IEEE International Electron Devices Meeting*, San Francisco, CA, Dec. 1988, pp.666-669.

[2] M. Mehregany, P. Nagarkar, S.D. Senturia, and J.H. Lang, "Operation of microfabricated harmonic and ordinary side-drive motors", *Proc. of the IEEE workshop of Micro Electro Mechanical Systems*, Napa Valley, CA, Feb. 1990, pp. 1-8.

[3] C.P. Taussig, "An Electrostatic Micromotor with Large In-plane Force and No Out-of-plane Force.", Hewlett-Packard Research Laboratories patent disclosure, 1997.

[4] T. Niino, T. Higuchi, and S. Egawa, "Dual Excitation Multiphase Electrostatic Drive", *Conference Record of the IEEE Industry Applications Conference,* Oct. 1995, pp. 1318-1325.

[5] N.K. Rao, D.K. Hartsfield, A. Purushotham, and S.L. Garverick, An IC for Closed-loop Micromotor Control, *Proc. of the 1995 International Symposium on Signals, Systems, and Electronics*, Oct. 1995, pp. 563-566.

[6] D.G. Leip, *Design and Implementation of a Capacitive Measurement Circuit with Application to Integrated Micromotor Position Sensing*, MIT M.S. Thesis in Electrical Engineering, Feb. 1994.

[7] P. Horowitz and W. Hill, *The Art of Electronics*, 2nd ed., Cambridge: Cambridge University Press, 1980, pp. 281-284.

Appendix A: Calculating the out-of-plane repulsive force density

This calculation was done by Carl Taussig to estimate the out-of-plane repulsive force density. It calculates force per area, and it is referred to in the text in Section 2.1.2, p. 5.

Figure A.1: Region considered in the calculation

Consider the rectangular region bounded by $x=+/-\pi/k$ and $y=+/- g/2$ as shown above. ($\pi/k=2d$ from Figure 2.3.) This box represents one spatial period of the motor. The dark lines represent the rotor and stator. To find the overall force density, we will first calculate the force (per length in the z direction) on the rotor generate by the fields within this box. Then, if we divide this by $4d=2\pi/k$, the spatial period, we will have the repulsive out-of-plane force density for the motor.

Boundary conditions

Assume that identical sine wave potential functions are imposed on both the rotor and stator. When the rotor and stator are aligned so their potentials are in phase, the maximum repulsive force is produced. This boundary condition is specified below.

Set $\phi = V\sin(kx)$ at $y=+g/2, -g/2$ (A-1)

Find $\phi(x,y)$ and $\overline{E}$

Since there is no charge between the plates, we know the potential ϕ must obey Laplace's equation. Therefore,

$\phi = A \sin(kx) \cosh(ky)$, where $A=V/\cosh(kg/2)$ (A-2)

$\overline{E} = -Ak[\cos(kx)\cosh(ky)i_x + \sin(kx)\sinh(ky)i_y]$ (A-3)

Calculate the energy in the electric field in the box

$$U = \frac{A^2 k^2 \varepsilon_0}{2} \int_{-\frac{g}{2}}^{\frac{g}{2}} \int_{\frac{\pi}{k}}^{\frac{\pi}{k}} (\cos^2 kx \cosh^2 ky + \sin^2 kx \cosh^2 ky) dx dy \qquad \text{(A-4)}$$

$$= \frac{A^2 k^2 \varepsilon_0}{4} \int_{-\frac{g}{2}}^{\frac{g}{2}} \int_{\frac{\pi}{k}}^{\frac{\pi}{k}} (\cos 2kx + \cosh 2ky) dx dy$$

$$= \frac{A \pi^2 \varepsilon_0}{2} \sinh kg$$

$$= V^2 \pi \varepsilon_0 \frac{\sinh \frac{kg}{2}}{\cosh \frac{kg}{2}}$$

Calculate the force at constant V in the gap direction (y-direction) per length in z

$$f_y = \frac{dU}{dg} \qquad \text{(A-5)}$$

$$= \frac{\pi \varepsilon_0 V^2 k}{2} \left(1 - \tanh^2 \frac{kg}{2}\right)$$

$$= \frac{\pi^2 \varepsilon_0 V_0^2}{4d} \left(1 - \tanh^2 \left(\frac{\pi g}{4d}\right)\right)$$

where $\pi/k = 2d$.

Calculate the force density

$$F_y = \frac{f_y}{4d} \qquad \text{(A-6)}$$

$$= \frac{\pi^2 \varepsilon_0 V_0^2}{16d^2} \left(1 - \tanh^2 \left(\frac{\pi g}{4d}\right)\right)$$

Appendix B: Calculating the in-plane force density

This calculation was based on the calculation in Appendix A, except this calculation finds the in-plane force density. It calculates force per area, and it is referred to in the text in Section 2.1.2, p. 5.
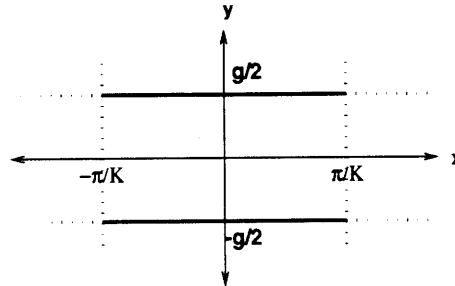

Figure A.1: Region considered in the calculation

Consider the rectangular region bounded by $x=+/-\pi/k$ and $y=+/-g/2$ as shown above. ($\pi/k=2d$ from Figure 2.3.) This box represents one spatial period of the motor. The dark lines represent the rotor and stator. To find the overall force density, we will first calculate the force (per length in the z direction) on the rotor generate by the fields within this box. Then, if we divide this by $4d=2\pi/k$, the spatial period, we will have the repulsive out-of-plane force density for the motor.

Boundary conditions

Assume that identical sine wave potential functions are imposed on both the rotor and stator.

Set $\phi = V\sin(kx)$ at y=-g/2   (B-1)

$\phi = V\sin(k(x-s))$ at y=+g/2   (B-2)

Find $\phi(x,y)$ and $\overline{E}$

Since there is no charge between the plates, we know the potential ϕ must obey Laplace's equation. Therefore,

ϕ=A[sin(kx)sinh(k(y-g/2)) - sin(k(x-s))sinh(k(y+d/2)], where A=V/sin(kg) (B-2)

$\overline{E}$=Ak[cos(kx)sinh(k(y-g/2)) - cos(k(x-s))sinh(k(y+g/2))]i$_x$

    + Ak[sin(kx)cosh(k(y-g/2) - sin(k(x-s)cosh(k(y+g/2)]i$_y$]   (B-3)

Calculate the energy in the electric field in the box

$$U = \frac{\varepsilon_0}{2}\int_{\frac{g}{2}}^{\frac{g}{2}} \int_{\frac{\pi}{k}}^{\frac{\pi}{k}} E^2 dx dy \tag{B-4}$$

$$= \frac{A^2\varepsilon_0}{2}\left[\left(\frac{\cosh kd}{2} - \cos ks\right)\sinh kd + 2kd\right]$$

Calculate the force at constant V in the in-plane direction (x-direction) per length in z

$$f_x = \frac{dU}{ds} \tag{B-5}$$

$$= \frac{\pi\varepsilon_0(VA)^2 k}{2}\sinh kd \sin ks$$

$$= \frac{\pi^2\varepsilon_0 V_0^2}{4d\sinh\frac{\pi d}{2d}}\sin\frac{\pi s}{2d}$$

where π/k=2d.

Calculate the force density

$$F_x = \frac{f_x}{4d} \tag{B-6}$$

$$= \frac{\pi^2\varepsilon_0 V_0^2}{16d^2\sinh\frac{\pi d}{2d}}\sin\frac{\pi s}{2d}$$

Appendix C: Circuit diagrams

This appendix contains all of the diagrams for the circuits that were built during the thesis. This includes the demodulator, the high-voltage circuitry, and the RC crossover network, which were discussed in Chapters 4, 5 and 6 respectively.

Bandpass

R1B

U6
1 LPa
2 BPa
3 N/AP/HPa
4 INVa
5 S1a
6 Sa/b
7 VA+
8 VD+
9 LSh
10 CLKa

LPb 20
BPb 19
N/AP/HPb 18
INVb 17
S1b 16
AGND 15
VA- 14
VD- 13
50/100 12
CLKb 11

R3A
R2A
From pre-amplifier
R1A

+8V
Cb
0

DSTM1
CLK

LMF100

R3B
R2B

-8V
Cb
0

Multiplier

U7
1 X1
2 X2
3 U0
4 U1
5 U2
6 Y1
7 Y2

VP 14
DD 13
W 12
Z1 11
Z2 10
ER 9
VN 8

+8V
Cb
LGND

R2
LGND

Cb
-8V
LGND

R1

AD734/AD

Lowpass Filter

C
0
R

U8
1 CLK_IN
2 CLK_R
3 LSh
4 V-

In 8
V+ 7
AGND 6
Out 5

+8V
Cb
AGND

-8V
Cb
0

LMF40

U9
3 +
V+
2 -
V-

+V
Cb
7
0

6
To MUX

4 1
Cb
-V
0

AD711/AD

R1F
R2F
0
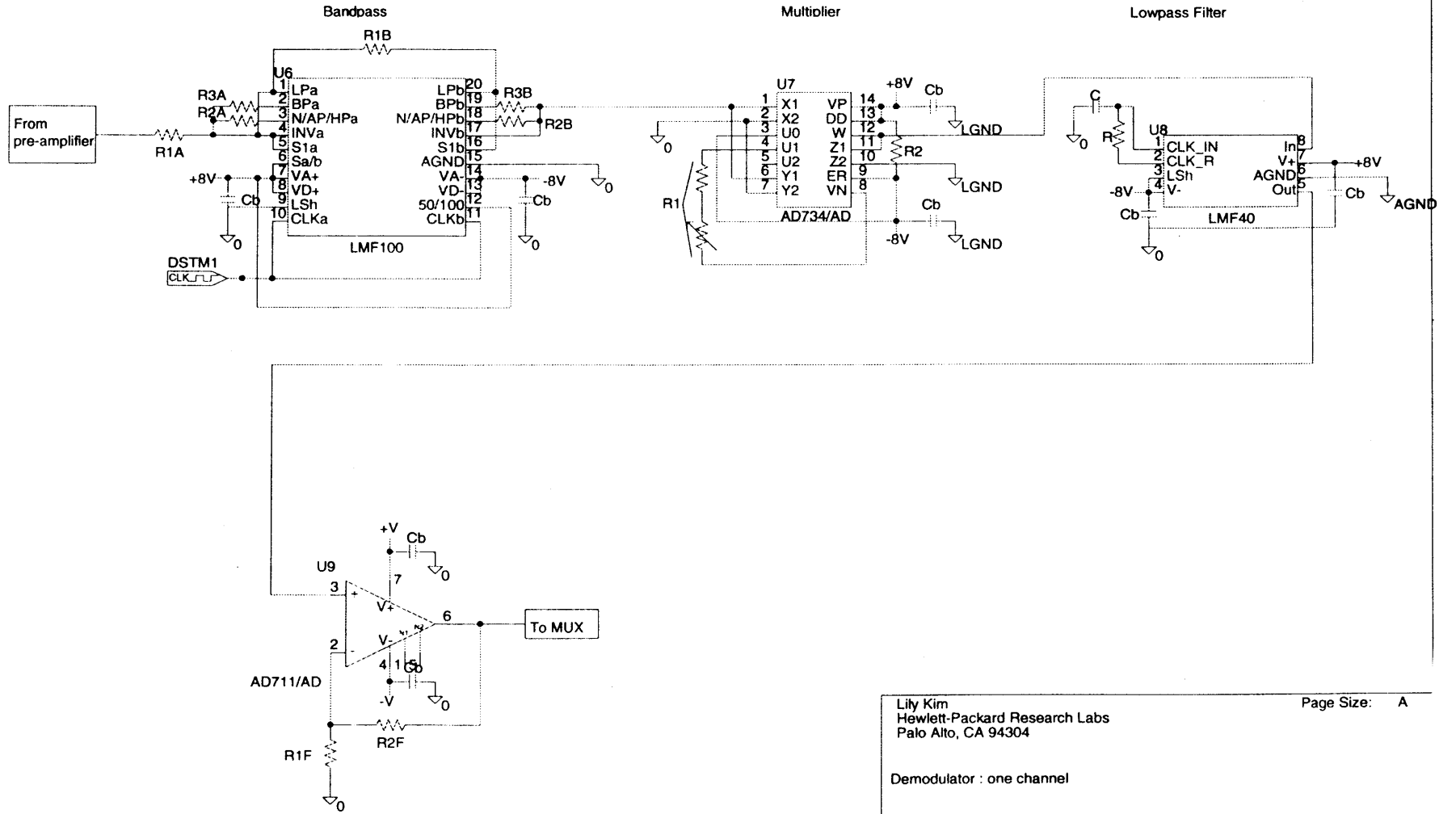
Page Size: A

Lily Kim
Hewlett-Packard Research Labs
Palo Alto, CA 94304

Demodulator board: this drawing includes everything on the
demodulator board except for the clock frequency chips
(Altera), which are shown on a separate page. The
demodulation channel is also shown on a separate page in
more detail.

December 17, 1997

Stator Phase A
(from RC
crossover)

R1

R2

+V   Cb

4 1 5

V-

6

V+

3

7 Cb

U10 AGND

AD711/AD

-V

One demodulation channel: f1

One demodulation channel: f2

Stator Phase B
(from RC
crossover)

R1

R2

+V   Cb

4 1 5

V-

6

V+

3

7 Cb

U12 AGND

AD711/AD

-V

One demodulation channel: f1

One demodulation channel: f2

Stator Phase C
(from RC
crossover)

R1

R2

+V   Cb

4 1 5

V-

6

V+

3

7 Cb

U13 AGND

AD711/AD

-V

One demodulation channel: f1

One demodulation channel: f2

Stator Phase D
(from RC
crossover)

R1

R2

+V   Cb

4 1 5

V-

6

V+

3

7 Cb

U14 AGND

AD711/AD

-V

One demodulation channel: f1

One demodulation channel: f2

Phase A signal to DSP

Phase B signal to DSP

Phase C signal to DSP

Phase D signal to DSP

U22
1 IN1   IN4 20
2 NO1   NO4 19
3 COM1   COM4 18
4 NC1   NC4 17
5 V-   V+ 16
6 GND   N.C. 15
7 NC2   NC3 14
8 COM2   COM3 13
9 NO2   NO3 12
10 IN2   IN3 11

MAX333A

-8V

Cb

+8V

Cb

Switch control (from DSP digital

CLOCK/DITHER SIGNAL

U19

+5V

Signal generator 1
0-5V
f=212*f1

nc4 7
nc5 8
nc6 9
GND3 10
nc7 11
nc8 12 0
nc9 13
nc10 14
VCC2 15 +5V
nc11 16
nc12 17

CLK_DIV

test9 40
test10 41
GND7 42
GND7 43
CLK_IN 44
GND6 1
GND1 2
VCC1 3
nc1 4
nc2 5
nc3 6

test8 39
nc20 38
test7 37
test6 36
VCC4 35 +5V
test5 34
nc19 33
nc18 32
test4 31
GN 30
test3 29

CLK_DIV_212
CLK_DIV_6
nc17
VCC3
GND4
nc16
nc15
nc14
nc13

test2 28
test1 27
26
25
24
23
22
21
20
19
18

+5V

DGND

Dither freq: to high-voltage circuitry: f1

CLK_LMF100_f

U18

+5V

Signal generator 2
0-5V
f=212*f2

nc4 7
nc5 8
nc6 9
GND3 10
nc7 11
nc8 12 0
nc9 13
nc10 14
VCC2 15 +5V
nc11 16
nc12 17

CLK_DIV

test9 40
test10 41
GND7 42
GND7 43
CLK_IN 44
GND6 1
GND1 2
VCC1 3
nc1 4
nc2 5
nc3 6

test8 39
nc20 38
test7 37
test6 36
VCC4 35 +5V
test5 34
nc19 33
nc18 32
test4 31
GN 30
test3 29

CLK_DIV_212
CLK_DIV_6
nc17
VCC3
GND4
nc16
nc15
nc14
nc13

test2 28
test1 27
26
25
24
23
22
21
20
19
18

+5V

DGND

Dither freq: to high-voltage circuitry:f2

CLK_LMF100_f2
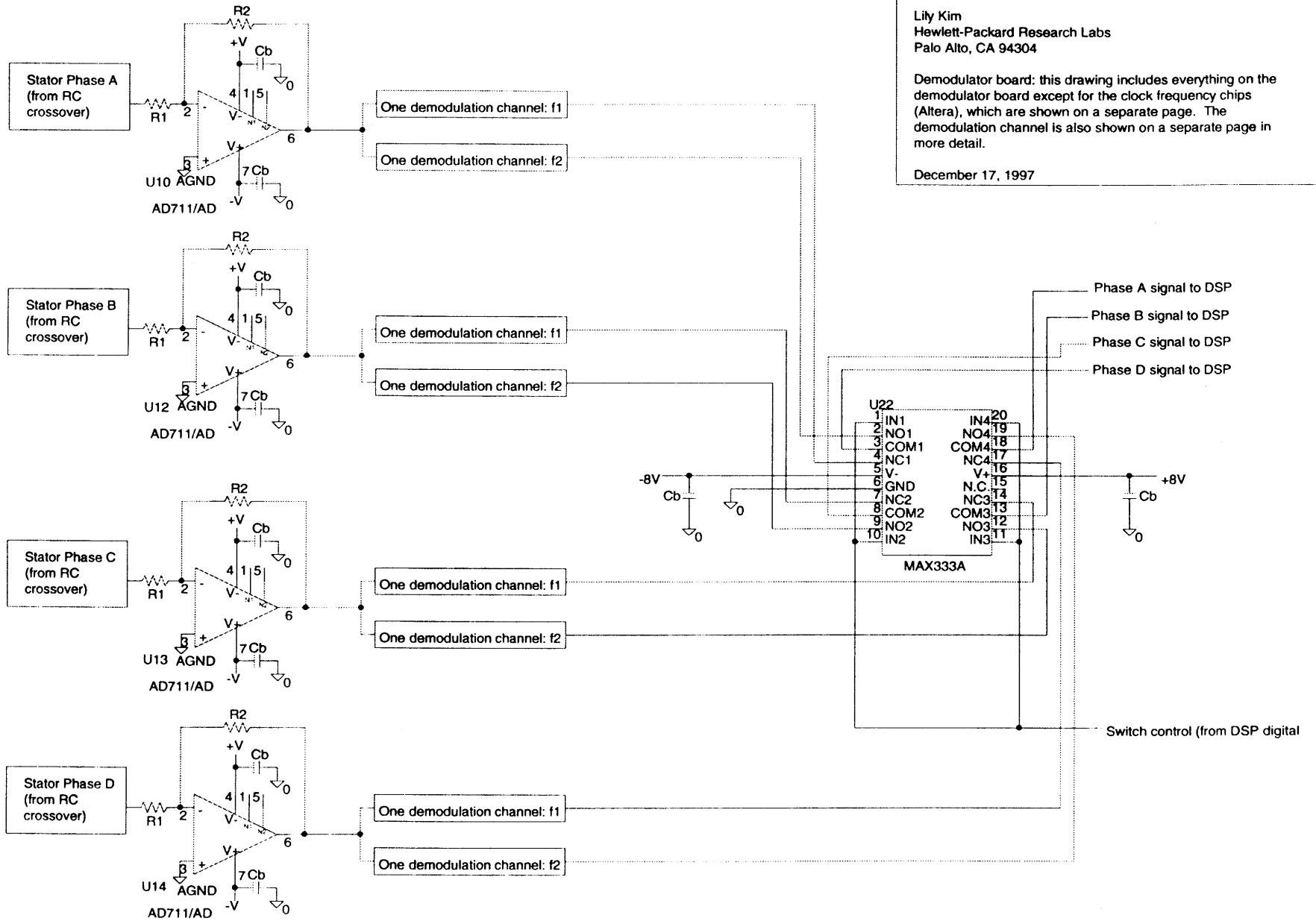
Lily Kim
Hewlett-Packard Research Labs
Palo Alto, CA 94304

Page Size: A

Clock/dither sources

Revision: -   December 17, 1997   Page   4   of   5
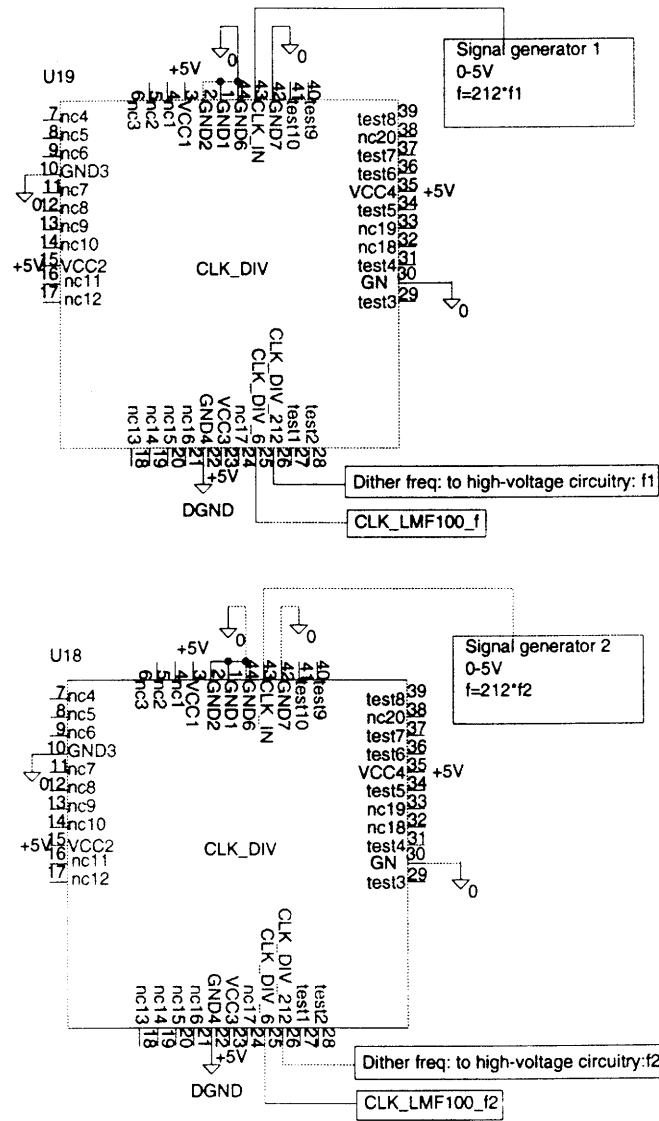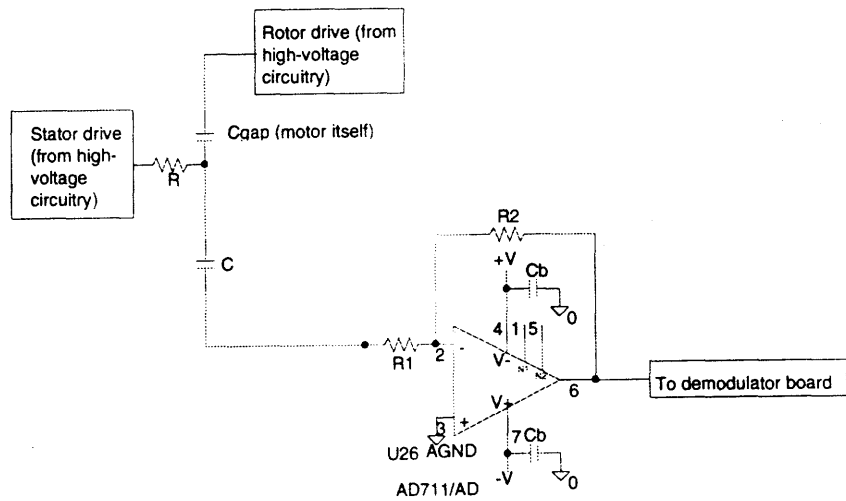
Rotor drive (from high-voltage circuitry)

Stator drive (from high-voltage circuitry)

Cgap (motor itself)

R

C

R2

+V   Cb

4 | 1 | 5

V-

R1   2

V+

6   To demodulator board

3

U26 AGND

7 Cb

AD711/AD   -V

Lily Kim
Hewlett-Packard Research Labs
Palo Alto, CA 94304

RC crossover network

Page Size: A

This circuit for one stator phase.
Four of these circuits are needed to
operate the motor, one for each stator
phase.

Revision: -   December 17, 1997   Page   5   of   5

Appendix D: Frequency-division program for Altera EPLD

This appendix contains the frequency-division program for the Altera part referred to in Section 4.3.4.

Clk_div.tdf

```
INCLUDE "lpm_counter.inc";
INCLUDE "lpm_compare";

% This file generates two different chips, depending on which constants are chosen%
%for NUM_DITHER_CYCLES AND NUM_FILTER_CYCLES. To choose an option, uncomment %
% appropriate lines %


%*********************%
%*   Option 1    *%
%*********************%
% This chip takes an input clock and divides it by 72 to approximate 102/(sqrt(2)) %
% this is the dither frequency output. the same clock is divided by 2 to provide the %
% clock for the maxim bandpass switched capacitor filter %

CONSTANT NUM_DITHER_CYCLES = H"48";
CONSTANT NUM_FILTER_CYCLES = H"2";


%*********************%
%*   Option 2    *%
%*********************%
% This chip takes an input clock divides it by 212 to approximate 300/(sqrt(2)) %
% this is dither frequency output. The same clock is divided by 6 to provide the %
% clock for the maxim bandpass switched capacitor filter %

%CONSTANT NUM_DITHER_CYCLES = H"6A"; %
%CONSTANT NUM_FILTER_CYCLES = H"3";%


% These constants are half the total division because the last divide-by-2 is done by %
% the dff which restores the duty cycle to 50%

SUBDESIGN clk_div
(
        clk_in                          :INPUT;
        clk_filter_out[2..0]            :OUTPUT;
        clk_dither_out[6..0]            :OUTPUT;
        clkdiv6                         :OUTPUT;
        clkdiv212                       :OUTPUT;
```

```
)

VARIABLE
        3bitcounter : lpm_counter WITH (LPM_WIDTH=3);
        7bitcounter : lpm_counter WITH (LPM_WIDTH=7);
        clk_dither_comp              : lpm_compare WITH (LPM_WIDTH=7,
LPM_PIPELINE=1,
                                        ONE_INPUT_IS_CONSTANT="YES");
        clk_filter_comp :lpm_compare WITH (LPM_WIDTH=3, LPM_PIPELINE=1,
                                        ONE_INPUT_IS_CONSTANT="YES");
        clk_dither_even              : dff;
        clk_filter_even    : dff;

BEGIN
        7bitcounter.clock=clk_in;
        clk_dither_out[] = 7bitcounter.q[];
        clk_dither_comp.clock=clk_in;
        clk_dither_comp.dataa[]=NUM_DITHER_CYCLES;
        clk_dither_comp.datab[]=clk_dither_out[6..0];
        7bitcounter.sload=clk_dither_comp.aeb;
        7bitcounter.data[]=H"02"; % this takes care of 2 extra clock cycles it takes to reload %
        clk_dither_even.d = not clk_dither.even.q;
        clk_dither_even.clk = clk_dither_comp.aeb;
        clkdiv212= clk_dither_even.q;
        3bitcounter.sload = clk_in;
        clk_filter_out[]=3bitcounter.q[];
        clk_filter_comp.clock=clk_in;
        clk_filter_comp.dataa[]=NUM_FILTER_CYCLES;
        clk_filter_comp.datab[]=clk_filter_out[2..0]
        3bitcounter.sload=clk_filter_comp.aeb;
        3bitcounter.data[]=H"02"; % this takes care of 2 extra clock cycles it takes to reload %
        clk_filter_even.d = not clk_filter_even.q;
        clk_filter_even.clk = clk_filter_comp.aeb;
        clkdiv6=clk_filter_even.q;
END;
```
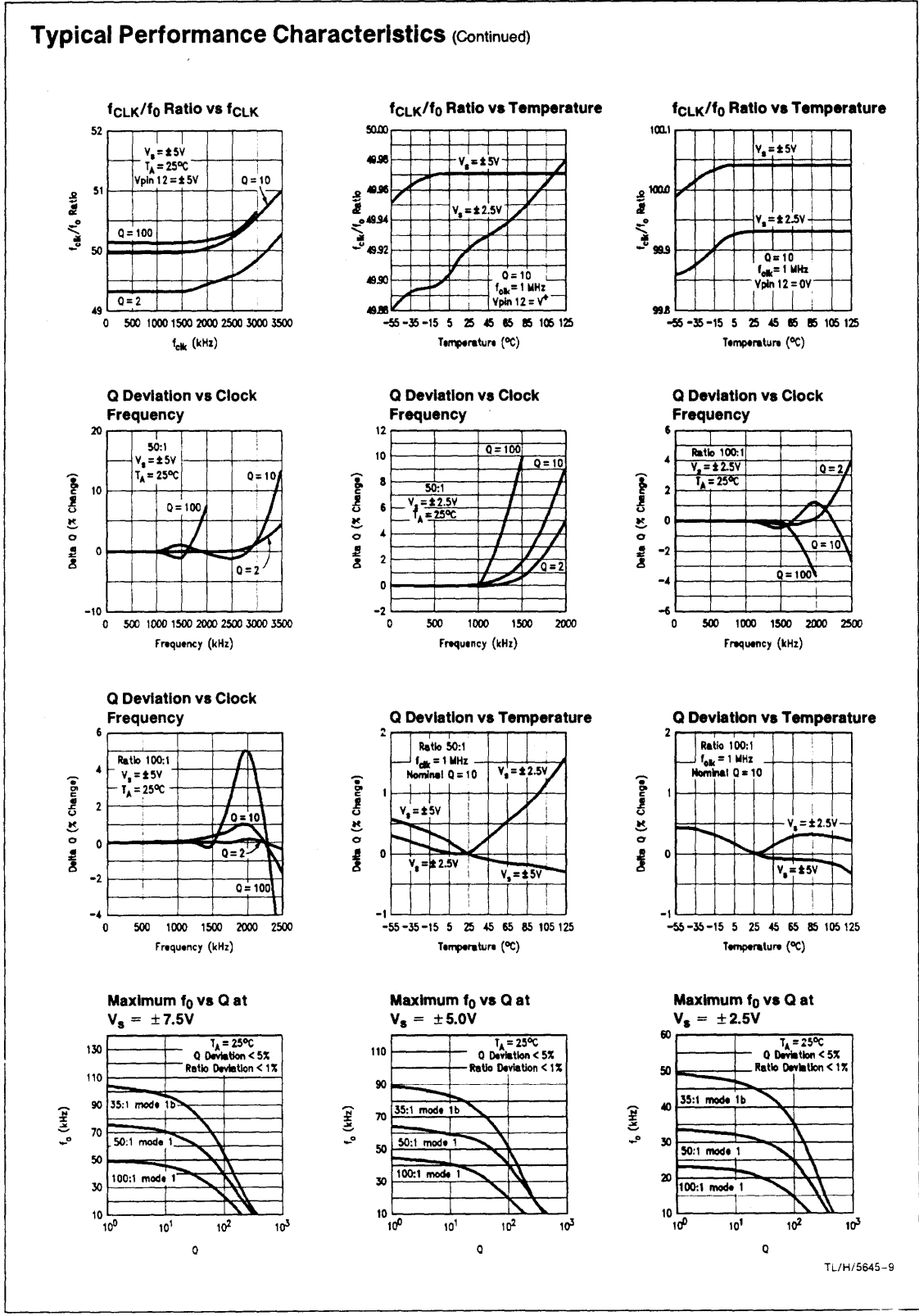
Appendix E: Excerpt from LMF100 data sheet

The following graph is from the data sheet for the LMF100 High Performance Dual Switched Capacitor Filter, made by National Semiconductor (1995). The graph shows the dependence of f_{clk}/f_0 on f_{clk}, and is referred to in Section 4.3.3 of the text.

Typical Performance Characteristics (Continued)

TL/H/5645–9